Extension of linear stability analysis for the dynamic stretching of plates: Spatio-temporal evolution of the perturbation

M. Xavier, C. Czarnota, D. Jouve, Sébastien Mercier, J.L. Dequiedt, A. Molinari

Version of Record: https://www.sciencedirect.com/science/article/pii/S0997753819300282
Manuscript_0942bc6e87c6c59bf772665786b692c1

Extension of linear stability analysis for the dynamic stretching of plates: spatio-temporal evolution of the perturbation.

M. Xavier[a,b,*], C. Czarnota[b], D. Jouve[a], S. Mercier[b], J.L. Dequiedt[a], A. Molinari[b]

[a] *CEA, DAM, DIF, 91297 Arpajon - FRANCE*
[b] *Laboratoire d'Etude des Microstructures et de Mécanique des Matériaux, LEM3 - UMR CNRS 7239, Université de Lorraine - CNRS - ENSAM 7 rue Felix Savart, 57070 METZ - FRANCE*

Abstract

Being able to predict fragment distributions in terms of speed and size, following the fracture of thin metallic shells subjected to dynamic expansion, is of major importance for civil and military applications. For ductile metals, this fracture process is initiated by plastic flow instability resulting in necking, i.e. the occurrence of local thinnings where the plastic deformation is localized. Since decades, linear stability analyses have been carried out to study the multiple necking formation via a perturbation of the fundamental state. The underlying assumption related to the linear stability analyses developed so far is the time scale separation (meaning that the development of the instability is larger than the evolution of the fundamental state), see C. Fressengeas and A. Molinari, Fragmentation of rapidly stretching sheets,

*Corresponding author
Email address: mathieu.xavier@cea.fr (M. Xavier)

Eur. J. Mech. A/Solids, 1994 or V. B. Shenoy and L. B. Freund, Necking bifurcations during high strain rate extension, J. Mech. Phys. Solids, 1999. The aim of the work is to propose an extended linear stability analysis which can tackle situations where the time scale separation hypothesis is no more satisfied (*i.e.* at very large strain large). The proposed methodology is exemplified by considering the dynamic extension of a plate under plain strain condition; the material behavior being modeled adopting various constitutive laws from rate insensitive to thermo-viscoplastic ones. The role of initial perturbation (or defect) is discussed. While the role of the initial conditions is important at the early stage of the deformation process, their influences on the growth rate and on the dominant mode are negligible at large strain for moderate loading rate. The benefit of the new theory is the fact that the spatio-temporal evolution of the mechanical and thermal parts of the perturbation can be captured naturally, even for cases where the plastic flow is initially stable and becomes unstable as the deformation progresses.
Keywords: Bifurcation, dynamic extension, Instability, multiple necking, thermo mechanical coupling

---

1. Introduction

Fragmentation of protective shells has been a subject of importance in military industry and civil engineering in the last decades. Metallic structures under intense loading may generate fragments with large residual velocities that could jeopardize safety around. Understanding the process that leads

to fragmentation becomes crucial, in order to prevent its occurrence.

This phenomenon has been studied experimentally in research laboratories on various geometries : cylinders (as in [39], [29], [10], [11] or [43]), rings (as in [28], [16], [23], [13] or [41]), or spherical and hemispherical shells (as in [37] or [24]). [28] has studied the dynamic deformation of copper and aluminum thin rings driven by a specific electromagnetic device. When the structures expand at high strain rates, multiple necking develops until the ring fails in multiple fragments. [12], [1] have made similar experiments and observed an enhanced ductility in the materials compared to the static case. The use of high speed cameras enables to analyse the expansion carefully, a collection of tests and data can be found in [41], [42]. Expansion driven by intense pressure loading created by an explosive charge is reported in [29] for a cylinder and in [24] for hemispherical shells. From all experiments, the failure process is divided into three steps. At the early stage of the expansion, deformation of the structure is homogeneous. Then, necking instabilities appear which generate local thinnings, triggering plastic strain localization. The last step is the fragmentation of the structure, see [41] for illustration by high quality images. The number of fracture sites is lower than the number of necks counted prior to failure. This is due to unloading waves whose propagation inhibits the growth of some necks.

Studies are not limited to experiments. [27] has proposed a probabilistic theory to investigate the fragmentation of metallic casings and his work has been extended by [13]. Both works predict a fragment size distribution,

consistent with experiments. However, in their approach, the process of multiple necking leading to fracture is disregarded. Bifurcation and stability analyses have also been used to study the development of necking instabilities. For rate independent behavior, an important contribution to this topic is due to [15] who have developed a quasi-static bifurcation analysis for a rectangular plate under plane strain tension. They have observed that under quasi-static loading, long wavelength modes are favored. [36] have extended [15] approach by taking into account inertia effects. They have developed a linear stability analysis of a rectangular plate, where a modal perturbation is superimposed to the fundamental solution (a material with infinite ductility that would never break). An important finding is that inertia tends to extinguish long wavelength modes. Due to multiaxiality of the plastic flow, combined with strain hardening (and strain rate sensitivity for rate sensitive materials), there is a cutting wavelength, *i.e* a minimum wavelength below which no necking instability can grow. Therefore, at any time during the deformation process, a particular mode is selected (the one presenting the maximum growth rate). In some contributions, this dominant mode is selected to scale the neck inter-spacing. The dynamic linear stability analysis of a rod can be found in [14], [25] or [44]. Plane strain loading analysis for rate independent material can also be found in [25], [20], while the linear stability analysis of the plate under biaxial loading with inertia effects can be found in [21]. Note that in [21], the effect of elasticity was also considered.

Ductile materials may exhibit strain rate effects. As a consequence, stabil-

ity analyses are also proposed in the literature for rate dependent materials. [17] characterized the stability of a rectangular plate under plane strain tension for quasi-static conditions. They have shown that the multidimensional nature of the flow damps short wavelength modes. [7, 8, 9] coupled viscous effects to inertia and observed that inertia slows down the growth of long wavelength perturbations. Therefore, the interplay between the stabilizing aspects of inertia, and the effect of viscous and multi-dimensional flow, leads to the selection of an intermediate wavelength, see also [25], [34]. The linear stability analysis has been also adopted to model the fragmentation of shaped charge jets. The fragment size predicted by linear stability analysis is consistent with experimental observations, [18, 31]. Since rings or tubes are expanded dynamically, the influence of the curvature on multiple necking development is investigated in [26]. It has been shown via a linear stability analysis that neck inter-spacing is not affected by the value of the tube radius when the tube is thin (for a ratio of wall thickness to mean radius below 0.01). So, a plate theory neglecting the curvature is able to provide accurate predictions for dynamic tube expansion or a rod configuration for the analysis of ring expansion.

[34] and [33] have illustrated, by coupling linear stability analysis and finite element calculations, that at very high strain rates, when inertia plays a dominant role in the loading process, a deterministic feature for the neck spacing is observed, leading to the development of an almost regular and uniform necking pattern. Finite Element calculations provide some addi-

tional insight which may explain theoretical and experimental results. [40] have simulated the stretching of unit cells presenting a geometrical defect of sinusoidal shape (initial length L_0, thickness h_0). They have observed that the neck development is strongly dependent upon the aspect ratio of the cells. This result corresponds to the selection of a particular wavelength, as observed in linear stability analysis. Simulations of ring expansions using the finite element method have been also performed in recent years, see [30, 2, 44, 35, 42, 34, 38]. From numerical simulations, it has been observed that fragment sizes are non-uniform as in experiments, but the mean spacing between two necks is quite consistent with the dominant mode predicted by the linear stability analysis. The role of defect amplitude on the fragmentation pattern of ductile materials is still debated in the literature today. [32] have investigated the development of defects in a dynamically loaded elastic bar. They have concluded that the localization process is, to a large part, influenced by the development of defects at an early stage of the stretching, at least before the force reaches a maximum. In the following, the strain corrresponding to the maximum force will be referred to as Considère strain. [38] have investigated the same configuration by Finite Element calculations. Stretching was simulated up to larger strain (larger than Considère's strain). They have clearly shown that defects evolve during the early stage of the deformation process, but the fracture pattern, originating from the necking process, is structured to a large extent beyond the Considère s strain by inertia effects. The interplay between modes having different relative ampli-

tudes and its role on the necking pattern has been investigated in [6] and [5] by accounting for the time evolution of random defects with various initial power spectrum. The probability density of neck spacing is derived in [5].

To the authors' best knowledge, all the stability analyses are based on a frozen coefficient theory. For a given time, the growth rate of a 2D or 3D perturbation with a given longitudinal mode is obtained assuming that the transversal modes do not evolve with time. In addition, as for 1D stability analysis, the time dependency of the perturbation is supposed of exponential form, linked to the instantaneous growth rate. These assumptions (frozen coefficient theory and exponential shape for the time dependency with a constant growth rate) are valid when the time scale inherited from the development of the necking is much smaller than the time scale of the background solution or equivalently when the growth rate of the perturbation is much larger than the background strain rate. When the time history of the perturbation is of interest, as in [9], [31], [6] or [38], the perturbation amplitude is updated from the integration of the instantaneous growth rate of the perturbation evaluated at each time step. This may lead to some approximations.

In this work, the assumption of frozen coefficient theory is no more adopted. A linear stability analysis is applied to a rectangular plate under plane strain loading. This configuration is representative of the dynamic expansion of a thin tube. In the second part (section 2.1), the position of the problem and the background flow (homogeneous solution of the problem) are described. In the third part (section 2.2), the main equations of the linear

stability analysis in plane strain are presented. Based on the new development, the frozen coefficient theory is no more necessary. Since this work is an extension of previous works of the literature, it is shown that when the material is viscoplastic and when the frozen coefficient theory is nevertheless imposed, the governing equations of the perturbation found in [25], [24] and [20] are retrieved. In section 3 the numerical method to solve the set of partial differential equations based on a spectral decomposition and the Tau method [22] are presented. Finally, in section 4, results concerning the temporal evolution of defects are presented. Various loading rates are considered. The predictions of the Linear stability analysis based on the frozen coefficient theory and the proposed approach are compared.

2. Modeling

2.1. Position of the problem: kinematics and background flow

In this section, the constitutive relations of the plastic flow in a plate subjected to dynamic extension under plane strain are established. A cartesian coordinate system is defined with respect to the orthonormal frame $(O, \mathbf{e}_1, \mathbf{e}_2, \mathbf{e}_3)$. The lagrangian (resp. current) position of a material particle is denoted by $\boldsymbol{X}$ (resp. $\boldsymbol{x}$). The displacement of a material particle is $\boldsymbol{u}(\boldsymbol{X}, t) = \boldsymbol{x}(\boldsymbol{X}, t) - \boldsymbol{X}$ and the velocity field is $\boldsymbol{v}(\boldsymbol{X}, t) = \partial \boldsymbol{u}(\boldsymbol{X}, t)/\partial t$, t being the time. For convenience, dependencies in $\boldsymbol{X}$ and t are intentionally omitted in the following. The deformation gradient tensor $\boldsymbol{F}$ is expressed as:

$$\boldsymbol{F} = \frac{\partial \boldsymbol{x}}{\partial \boldsymbol{X}} \,. \tag{1}$$

The plate, centered on O, is of initial length $2L_{01}$, initial thickness $2L_{03}$, and is infinite along the x_2 direction, such that $x_2 = X_2$ (plane strain condition). A uniform time independent velocity field $\pm V_{01}\mathbf{e}_1$ is imposed at $X_1 = \pm L_{01}$, see Fig. 1.

The material is assumed isotropic, incompressible and rigid plastic. Since

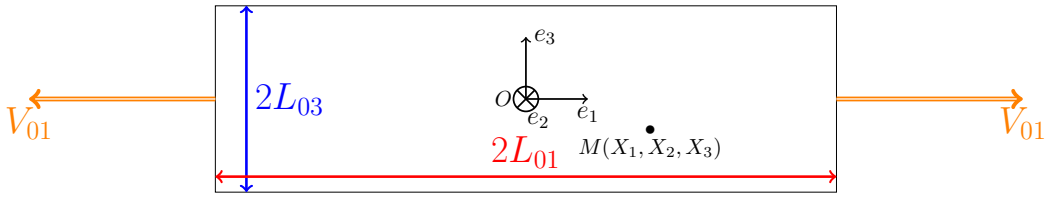

Figure 1: Plate configuration. Initially, the plate has a length of $2L_{01}$ and a thickness of $2L_{03}$. Velocity V_{01} is applied at the two opposite sides ($X_1 = \pm L_{01}$). Plane strain conditions are considered.

elasticity is neglected, the plastic strain rate tensor is obtained from the deformation gradient tensor as:

$$\boldsymbol{D} = \frac{1}{2}\left(\dot{\boldsymbol{F}}\boldsymbol{F}^{-1} + \boldsymbol{F}^{-\mathrm{T}}\dot{\boldsymbol{F}}^{\mathrm{T}}\right) \,, \tag{2}$$

where the overdot is the time derivative operator and $(\cdot)^{\mathrm{T}}$ stands for the transpose of the second order tensor $(\cdot)$. $(\cdot)^{-\mathrm{T}}$ stands for the inverse of $(\cdot)^{\mathrm{T}}$. The yield function Φ is defined as :

$$\Phi = \bar{\sigma} - Y \,, \tag{3}$$

$\bar{\sigma} = \sqrt{\frac{3}{2}\mathbf{S} : \mathbf{S}}$ being the effective stress and Y the flow stress of the material. $\mathbf{S}$ is the deviatoric part of the Cauchy stress tensor $\mathbf{\Sigma}$ and (:) denotes the inner product of second order tensors. In the present work, the material is viscoplastic and thermal sensitivity is included. In its general form, the flow stress is written as:

$$Y = f(\varepsilon_p, \dot{\varepsilon}_p, \theta)\,, \tag{4}$$

where θ is the temperature. $\dot{\varepsilon}_p$ and ε_p denote the effective plastic strain rate and the accumulated plastic strain, respectively. They are related to the plastic strain rate tensor $\mathbf{D}$:

$$\dot{\varepsilon}_p = \sqrt{\frac{2}{3}\mathbf{D} : \mathbf{D}}\,, \tag{5a}$$

$$\varepsilon_p = \int_0^t \dot{\varepsilon}_p d\tau. \tag{5b}$$

During the dynamic extension of the plate, viscoplastic flow occurs, so $\Phi = 0$. As a consequence, from Eq. (3), $\bar{\sigma} = Y$ and the J_2 flow theory, used to describe viscoplastic flow, leads to:

$$\mathbf{D} = \frac{3\dot{\varepsilon}_p}{2\bar{\sigma}}\mathbf{S} = \frac{3\dot{\varepsilon}_p}{2Y}\mathbf{S}\,. \tag{6}$$

In this section, the homogeneous solution of the dynamic problem, referred to as background solution or background state in the following, is

first derived. The conservation of linear momentum in the Lagrangian frame reads:

$$\text{div } \mathbf{T} = \rho \mathbf{\Gamma} \tag{7}$$

where div stands for the divergence operator, $\mathbf{\Gamma}$ denotes the acceleration vector and ρ is the mass density. The nominal stress tensor $\mathbf{T}$ is related to the Cauchy stress tensor $\mathbf{\Sigma}$ and the deformation gradient $\mathbf{F}$ through the relation:

$$\mathbf{T} = \det(\mathbf{F})\mathbf{F^{-1}\Sigma} = \mathbf{F^{-1}\Sigma} \tag{8}$$

where $\det(\mathbf{F}) = 1$ has been used due to incompressibility, $\det(\cdot)$ standing for the determinant of the second order tensor $(\cdot)$.

Dynamic loadings are considered, generating large strain rates during the plastic straining. Therefore, adiabatic conditions may be assumed and the corresponding heat equation is written as:

$$\dot{\theta} = \frac{Y\dot{\varepsilon}_p}{\rho C}\,, \tag{9}$$

where C, assumed constant, is the specific heat capacity at constant volume. Eq. (9) has been obtained considering that the plastic work is totally converted into heat.

The boundary conditions prescribed at the plate depicted in Fig. 1 (*i.e.*

at $X_1 = \pm L_{01}$ and $X_3 = \pm L_{03}$) are :

$$v_1(\pm L_{01}, X_3, t) = \pm V_{01} \quad T_{13}(\pm L_{01}, X_3, t) = 0 \tag{10}$$

$$T_{33}(X_1, \pm L_{03}, t) = 0 \quad T_{31}(X_1, \pm L_{03}, t) = 0\,. \tag{11}$$

The background solution, for which all related quantities will be denoted with a superscript (b), is summarized below (see e.g. [9] for more details).

Owing to incompressibility and due to the constant velocity applied at $X_1 = \pm L_{01}$, the background deformation gradient tensor $\mathbf{F^{(b)}}$ given by Eq. (1), is written under plane strain loading as:

$$\mathbf{F^{(b)}} = \begin{pmatrix} 1+\varepsilon_{11} & 0 & 0 \\ 0 & 1 & 0 \\ 0 & 0 & \dfrac{1}{1+\varepsilon_{11}} \end{pmatrix} \tag{12}$$

with:

$$\varepsilon_{11} = \dot{\varepsilon}_{11} t = \frac{V_{01}}{L_{01}} t\,. \tag{13}$$

The resulting background strain rate tensor $\mathbf{D^{(b)}}$ is then obtained from Eq. (2):

$$\mathbf{D^{(b)}} = \begin{pmatrix} \dfrac{\dot{\varepsilon}_{11}}{1+\varepsilon_{11}} & 0 & 0 \\ 0 & 0 & 0 \\ 0 & 0 & -\dfrac{\dot{\varepsilon}_{11}}{1+\varepsilon_{11}} \end{pmatrix}. \tag{14}$$

The background Cauchy stress tensor $\mathbf{\Sigma^{(b)}}$, satisfying Eq.(7), is given as in

[9] or [20] by:

$$\mathbf{\Sigma^{(b)}} = \begin{pmatrix} \dfrac{2Y^{(b)}}{\sqrt{3}} - P^I & 0 & 0 \\ 0 & \dfrac{Y^{(b)}}{\sqrt{3}} - P^I & 0 \\ 0 & 0 & -P^I \end{pmatrix} \tag{15}$$

with the inertial pressure P^I given by:

$$P^I = \rho \frac{\dot{\varepsilon}_{11}^2 (L_{03}^2 - X_3^2)}{(1+\varepsilon_{11})^4} \tag{16}$$

As observed in experiments (*e.g.* [1]), perturbations that may develop during dynamic deformation of ductile materials are related to the occurrence of multiple necks and fragmentation. The goal of the present work is to estimate the time evolution of an imperfection, through an extension of the classical linear stability analysis which will be detailed in the forthcoming section.

2.2. Extension of the classical Linear Stability Analysis

Our approach is obtained following the formalism of [36], [25], [24] or [20]. At a given time $t_0 = 0$, a time dependent perturbation is added to the background solution such that any variable (scalar, vector or second order tensor) G, solution of the perturbed problem, is the sum of two terms:

$$G = G^{(b)} + \delta G \tag{17}$$

where $G^{(b)}$ is the background state of the field G (see previous section) and δG is the associated perturbation field.

Owing to plane strain loading, the perturbation in position $\delta\boldsymbol{x}$ is written in the orthonormal frame ($\mathbf{e}_1$, $\mathbf{e}_2$, $\mathbf{e}_3$) as:

$$\delta\boldsymbol{x} = \delta x_1(X_1, X_3, t)\mathbf{e}_1 + \delta x_3(X_1, X_3, t)\mathbf{e}_3 \tag{18}$$

From Eqs (1) and (18), the perturbed deformation gradient tensor is therefore:

$$\delta\mathbf{F} = \begin{bmatrix} \delta x_{1,1} & 0 & \delta x_{1,3} \\ 0 & 0 & 0 \\ \delta x_{3,1} & 0 & \delta x_{3,3} \end{bmatrix} \tag{19}$$

where the comma has been used for the partial derivative with respect to the lagrangian position: $A_{,j} = \partial A/\partial X_j$ for any scalar A.

Since the material is assumed incompressible ($\det(\mathbf{F}^{(b)} + \delta\mathbf{F}) = 1$), a combination of Eqs (12) and (19) leads to the following relationship:

$$\delta x_{1,1}\frac{1}{1+\varepsilon_{11}} + \delta x_{3,3}(1+\varepsilon_{11}) = 0 \tag{20}$$

As in [9] or [24], a stream function $\delta\psi$ is introduced to represent the perturbed position:

$$\delta x_1 = -(1+\varepsilon_{11})\delta\psi_{,3} \quad , \quad \delta x_3 = \frac{1}{(1+\varepsilon_{11})}\delta\psi_{,1} \tag{21}$$

The perturbed strain rate tensor components are obtained from Eqs (2,12,19,21):

$$\delta D_{13} = \frac{1}{2}\left[\delta\dot{\psi}_{,11}\frac{1}{(1+\varepsilon_{11})^2} - \delta\dot{\psi}_{,33}(1+\varepsilon_{11})^2\right], \tag{22a}$$

$$\delta D_{11} = -\delta\dot{\psi}_{,31}, \tag{22b}$$

$$\delta D_{33} = -\delta D_{11}, \tag{22c}$$

$$\delta D_{12} = \delta D_{22} = \delta D_{23} = 0. \tag{22d}$$

From Eq. (8), disturbance of the nominal stress tensor $\delta\mathbf{T} = \mathbf{F^{(b)^{-1}}}\left(-\delta\mathbf{F}\mathbf{F^{(b)^{-1}}}\boldsymbol{\Sigma^{(b)}} + \delta\boldsymbol{\Sigma}\right)$ is related to the deviator $\delta\mathbf{S}$ of the perturbed Cauchy stress tensor $\delta\boldsymbol{\Sigma}$, the perturbed position $\delta\mathbf{x}$ and the perturbed pressure δP:

$$\delta T_{13} = P^I\delta x_{1,3} + \delta S_{13}\frac{1}{1+\varepsilon_{11}} \quad \delta T_{31} = -\left(\frac{2Y^{(b)}}{\sqrt{3}} - P^I\right)\delta x_{3,1} + \delta S_{31}\,(1+\varepsilon_{11}) \tag{23a}$$

$$\delta T_{11} = -\left(\frac{2Y^{(b)}}{\sqrt{3}} - P^I\right)\delta x_{1,1}\frac{1}{(1+\varepsilon_{11})^2} + \frac{1}{1+\varepsilon_{11}}(\delta S_{11} - \delta P) \tag{23b}$$

$$\delta T_{33} = P^I(1+\varepsilon_{11})^2\delta x_{3,3} + (\delta S_{33} - \delta P)(1+\varepsilon_{11}) \tag{23c}$$

with $\delta P = -\frac{1}{3}\mathrm{tr}(\delta\boldsymbol{\Sigma})$, $\mathrm{tr}(\cdot)$ standing for the trace operator of the second order tensor $(\cdot)$.

Next, all perturbed quantities will be expressed in terms of the stream function $\delta\psi$ and the perturbed temperature $\delta\theta$. Finally, a system of equations describing the evolution of the two perturbed unknowns $\delta\psi$ and $\delta\theta$ will be derived.

The perturbation in plastic strain rate is determined by combining Eqs(5a,14,22b-22c):

$$\delta\dot{\varepsilon}_p = -\frac{2}{\sqrt{3}}\delta\dot{\psi}_{,13} \tag{24}$$

The perturbed plastic strain is defined upon integration with respect to time of Eq. (24), see Eq. (5b):

$$\delta\varepsilon_p - \delta\varepsilon_p^0 = -\frac{2}{\sqrt{3}}\left(\delta\psi_{,13} - \delta\psi_{,13}^0\right) \tag{25}$$

where $\delta\varepsilon_p^0$ and $\delta\psi_{,13}^0$ are initial quantities (specified values at time t_0) for the perturbed quantities $\delta\varepsilon_p$ and $\delta\psi_{,13}$. In the following, the case where $\delta\varepsilon_p^0 = -2/\sqrt{3}\delta\psi_{,13}^0$ is considered. The derivation of the present model (see the continuation of the theory) could have been carried out without this assumption. No relationship is necessary for these quantities but since they are both representative of the initial perturbation in strain, any other choice does not seem natural. Therefore, one finally obtains:

$$\delta\varepsilon_p = -\frac{2}{\sqrt{3}}\delta\psi_{,13} \tag{26}$$

From the J_2 flow law (6) and the perturbed strain rate tensor given by Eq.(22), the perturbation $\delta\mathbf{S}$ of the deviatoric part of the Cauchy stress tensor is expressed in terms of the stream function :

$$\delta S_{13} = \frac{Y^{(b)}}{3\dot{\varepsilon}_p^{(b)}} \left[\frac{1}{(1+\varepsilon_{11})^2} \delta\dot{\psi}_{,11} - (1+\varepsilon_{11})^2 \delta\dot{\psi}_{,33} \right] \tag{27a}$$

$$\delta S_{11} = -\frac{2}{3}\delta\dot{\psi}_{,13} Y^{(b)}_{,\dot{\varepsilon}_p} - \frac{2}{3}\delta\psi_{,13} Y^{(b)}_{,\varepsilon_p} + \delta\theta \frac{Y^{(b)}_{,\theta}}{\sqrt{3}} \tag{27b}$$

$$\delta S_{33} = -\delta S_{11} \tag{27c}$$

$$\delta S_{12} = \delta S_{22} = \delta S_{23} = 0 \tag{27d}$$

with[1]

$$\delta Y = \delta\varepsilon_p Y^{(b)}_{,\varepsilon_p} + \delta\dot{\varepsilon}_p Y^{(b)}_{,\dot{\varepsilon}_p} + \delta\theta Y^{(b)}_{,\theta} \tag{28}$$

With the introduction of Eqs(21,27) into Eqs(23) together with the linearization of the conservation of momentum equation Eq.(7), and after elimination of the pressure perturbation δP using a cross-derivation, a fourth order partial differential equation for the stream function $\delta\psi$ is found :

$$\begin{aligned}
&\rho \left[-(1+\varepsilon_{11})^2 \delta\ddot{\psi}_{,33} - \frac{1}{(1+\varepsilon_{11})^2}\delta\ddot{\psi}_{,11} + 2\frac{\dot{\varepsilon}_{11}}{(1+\varepsilon_{11})^3}\delta\dot{\psi}_{,11} - 2(1+\varepsilon_{11})\dot{\varepsilon}_{11}\delta\dot{\psi}_{,33} \right] \\
&= -\frac{Y^{(b)}}{3\dot{\varepsilon}_p^{(b)}} \left[(1+\varepsilon_{11})^4 \delta\dot{\psi}_{,3333} + \frac{1}{(1+\varepsilon_{11})^4}\delta\dot{\psi}_{,1111} \right] - \frac{2}{3}\left[2Y^{(b)}_{,\dot{\varepsilon}_p} - \frac{Y^{(b)}}{\dot{\varepsilon}_p^{(b)}} \right] \delta\dot{\psi}_{,1313} \\
&\quad - \frac{4Y^{(b)}_{,\varepsilon_p}}{3}\delta\psi_{,1313} + \frac{2Y^{(b)}_{,\theta}}{\sqrt{3}}\delta\theta_{,13}
\end{aligned} \tag{29}$$

[1] $Y_{,\alpha} = \dfrac{\partial Y}{\partial \alpha}$ with ($\alpha = \varepsilon_p$, $\dot{\varepsilon}_p$ or θ)

It is important to notice that the perturbation in temperature is present in this equation, because of the thermo-mechanical coupling. The evolution law of the perturbation in temperature $\delta\theta$ is derived from Eq. (9):

$$\rho C \delta\dot{\theta} = \dot{\varepsilon}_p^{(b)} \left(\delta\varepsilon_p Y_{,\varepsilon_p}^{(b)} + \delta\dot{\varepsilon}_p Y_{,\dot{\varepsilon}_p}^{(b)} + \delta\theta Y_{,\theta}^{(b)} \right) + \delta\dot{\varepsilon}_p Y^{(b)} \tag{30}$$

This relationship can also be written in terms of the stream function $\delta\psi$:

$$\rho C \delta\dot{\theta} = -\frac{2}{\sqrt{3}} \delta\psi_{,13} Y_{,\varepsilon_p}^{(b)} \dot{\varepsilon}_p^{(b)} - \frac{2}{\sqrt{3}} \left[Y_{,\dot{\varepsilon}_p}^{(b)} \dot{\varepsilon}_p^{(b)} + Y^{(b)} \right] \delta\dot{\psi}_{,13} + \delta\theta Y_{,\theta}^{(b)} \dot{\varepsilon}_p^{(b)} \tag{31}$$

The system formed by Eqs (29) and (31) has to be complemented with the boundary conditions, see Eq. (10) and Eq. (11) :

$$\delta v_1(\pm L_{01}, X_3, t) = 0 \quad \delta T_{13}(\pm L_{01}, X_3, t) = 0 \tag{32}$$

$$\delta T_{31}(X_1, \pm L_{03}, t) = 0 \quad \delta T_{33}(X_1, \pm L_{03}, t) = 0\,. \tag{33}$$

Eq. (33) provides two additional relationships (the first one related to shear stress and the second one related to normal stress) for the stream function $\delta\psi$ and the perturbed temperature $\delta\theta$:

$$-\frac{2Y^{(b)}}{\sqrt{3}} \frac{1}{1+\varepsilon_{11}} \delta\psi_{,11} + \frac{Y^{(b)}}{3\dot{\varepsilon}_p^{(b)}} \left[\frac{1}{1+\varepsilon_{11}} \delta\dot{\psi}_{,11} - (1+\varepsilon_{11})^3 \delta\dot{\psi}_{,33} \right] = 0 \quad \text{at } X_3 = \pm L_{03} \tag{34}$$

$$\rho\left[-\delta\ddot{\psi}_{,3}(1+\varepsilon_{11})-2\dot{\varepsilon}_{11}\delta\dot{\psi}_{,3}\right]=\frac{Y^{(b)}}{3\dot{\varepsilon}_p^{(b)}}\left[\frac{1}{1+\varepsilon_{11}}\delta\dot{\psi}_{,113}-(1+\varepsilon_{11})^3\delta\dot{\psi}_{,333}\right]-\frac{4Y^{(b)}_{,\dot{\varepsilon}_p}}{3(1+\varepsilon_{11})}\delta\dot{\psi}_{,113}$$
$$-\frac{4Y^{(b)}_{,\varepsilon_p}}{3(1+\varepsilon_{11})}\delta\psi_{,113}+\delta\theta_{,1}\frac{2Y^{(b)}_{,\theta}}{\sqrt{3}(1+\varepsilon_{11})}$$
$$\mp\frac{2\rho L_{03}\dot{\varepsilon}_{11}^2}{(1+\varepsilon_{11})^5}\delta\psi_{,11}\quad\text{at } X_3=\pm L_{03}\tag{35}$$

In the literature (see [24] or [19]), perturbation modes are searched of the general form:

$$\delta\psi=\sin\left(\gamma_1 X_1\right)\hat{\psi}(X_3,t)\,,\tag{36}$$

and, based on Eq. (29), $\delta\theta$ must be expressed as follows:

$$\delta\theta=\cos(\gamma_1 X_1)\hat{\theta}(X_3,t)\,.\tag{37}$$

γ_1 is the Lagrangian longitudinal wavenumber; $\hat{\psi}(X_3,t)$ and $\hat{\theta}(X_3,t)$ are two unknown functions representative of the thermomechanical perturbation. From Eqs (36-37), the boundary conditions (32) are satisfied when the wavenumber γ_1 verifies:

$$\gamma_1 L_{01}=i_1\pi\tag{38}$$

where i_1, named wavenumber index in the following, is an integer which determines the number of initial necks induced by the perturbation. Combining the prescribed definition of the stream function (36) with Eq. (21),

the perturbed position is found:

$$\delta x_1 = -(1+\varepsilon_{11})\sin(\gamma_1 X_1)\hat{\psi}_{,3}(X_3,t) \quad \delta x_3 = \frac{\gamma_1}{1+\varepsilon_{11}}\cos(\gamma_1 X_1)\hat{\psi}(X_3,t) \quad (39)$$

At this stage, it has not been possible to obtain closed form expressions for $\hat{\psi}(X_3,t)$ and $\hat{\theta}(X_3,t)$, solution of the problem (29) and (31). So a numerical method is needed and is exemplified in the next section.

Next we introduce the dimensionless variable $\tilde{X}_3$ defined by:

$$\tilde{X}_3 = X_3/L_{03} \quad (40)$$

and the new unknowns $\tilde{\psi}$ and $\tilde{\theta}$ written as:

$$\tilde{\psi}(\tilde{X}_3,t) = \hat{\psi}(X_3,t)\,, \quad \tilde{\theta}(\tilde{X}_3,t) = \hat{\theta}(X_3,t)\,. \quad (41)$$

In the following, the notation $(.)_{,3}$ will refer to two different definitions depending on the associated coordinate; for a function $\hat{G}(X_3,t)$ (resp. $\tilde{G}(\tilde{X}_3,t)$) then $\hat{G}_{,3}$ (resp. $\tilde{G}_{,3}$) is representative of the partial derivative of $\hat{G}$ (resp. $\tilde{G}$) relatively to X_3 (resp. $\tilde{X}_3$). As a consequence, $\tilde{\psi}_{,3} = \partial\tilde{\psi}/\partial\tilde{X}_3 = L_{03}\hat{\psi}_{,3}$.

Combining Eqs (29,31,36-37,40-41), the following system of differential

equations for $\tilde{\psi}$ and $\tilde{\theta}$ is obtained :

$$\frac{a_1}{L_{03}^2}\ddot{\tilde{\psi}}_{,33} + a_2\ddot{\tilde{\psi}} + \frac{a_3}{L_{03}^4}\dot{\tilde{\psi}}_{,3333} + \frac{a_4}{L_{03}^2}\dot{\tilde{\psi}}_{,33} + a_5\dot{\tilde{\psi}} + \frac{a_6}{L_{03}^2}\tilde{\psi}_{,33} + \frac{a_7}{L_{03}}\tilde{\theta}_{,3} = 0 \quad (42a)$$

$$\dot{\tilde{\theta}} + b_1\tilde{\theta} + \frac{b_2}{L_{03}}\dot{\tilde{\psi}}_{,3} + \frac{b_3}{L_{03}}\tilde{\psi}_{,3} = 0 \quad (42b)$$

with:

$$\begin{aligned}
a_1(t) &= -\rho(1+\varepsilon_{11})^2 & a_2(t) &= \rho\tfrac{\gamma_1^2}{(1+\varepsilon_{11})^2} \\
a_3(t) &= \frac{Y^{(b)}}{3\dot{\varepsilon}_p^{(b)}}(1+\varepsilon_{11})^4 & a_4(t) &= -2\rho(1+\varepsilon_{11})\dot{\varepsilon}_{11} - \frac{2\gamma_1^2}{3}\left[2Y_{,\dot{\varepsilon}_p}^{(b)} - \frac{Y^{(b)}}{\dot{\varepsilon}_p^{(b)}}\right] \\
a_5(t) &= -2\rho\frac{\gamma_1^2\dot{\varepsilon}_{11}}{(1+\varepsilon_{11})^3} + \frac{Y^{(b)}}{3\dot{\varepsilon}_p^{(b)}}\frac{\gamma_1^4}{(1+\varepsilon_{11})^4} & a_6(t) &= -\frac{4Y_{,\varepsilon_p}^{(b)}}{3}\gamma_1^2 \\
a_7(t) &= \frac{2Y_{,\theta}^{(b)}}{\sqrt{3}}\gamma_1 & b_1(t) &= -\frac{Y_{,\theta}^{(b)}\dot{\varepsilon}_p^{(b)}}{\rho C} \\
b_2(t) &= \tfrac{2}{\sqrt{3}}\tfrac{\gamma_1}{\rho C}\left[Y_{,\dot{\varepsilon}_p}^{(b)}\dot{\varepsilon}_p^{(b)} + Y^{(b)}\right] & b_3(t) &= \frac{2}{\sqrt{3}}\frac{\gamma_1}{\rho C}Y_{,\varepsilon_p}^{(b)}\dot{\varepsilon}_p^{(b)}
\end{aligned} \quad (43)$$

Boundary conditions (34) and (35), valid for $\tilde{X}_3 = \pm 1$, become:

$$\frac{1}{L_{03}^2}\dot{\tilde{\psi}}_{,33} + c_1\dot{\tilde{\psi}} - \gamma_1 c_2\tilde{\psi} = 0 \quad (44a)$$

$$\frac{n_1}{L_{03}}\ddot{\tilde{\psi}}_{,3} + \frac{n_2}{L_{03}^3}\dot{\tilde{\psi}}_{,333} + \frac{n_3}{L_{03}}\dot{\tilde{\psi}}_{,3} + \frac{n_4}{L_{03}}\tilde{\psi}_{,3} + n_5\tilde{\psi} + n_6\tilde{\theta} = 0 \quad (44b)$$

where:

$$
\begin{aligned}
c_1(t) &= \frac{\gamma_1^2}{(1+\varepsilon_{11})^4} & c_2(t) &= 2\sqrt{3}\dot{\varepsilon}_p^{(b)}\frac{\gamma_1}{(1+\varepsilon_{11})^4} \\
n_1(t) &= -\rho(1+\varepsilon_{11}) & n_2(t) &= \frac{Y^{(b)}}{3\dot{\varepsilon}_p^{(b)}}(1+\varepsilon_{11})^3 \\
n_3(t) &= -2\rho\dot{\varepsilon}_{11} + \frac{Y^{(b)}}{3\dot{\varepsilon}_p^{(b)}(1+\varepsilon_{11})}\gamma_1^2 - \frac{4Y^{(b)}_{,\dot{\varepsilon}_p}}{3(1+\varepsilon_{11})}\gamma_1^2 & n_4(t) &= -\frac{4Y^{(b)}_{,\varepsilon_p}}{3(1+\varepsilon_{11})}\gamma_1^2 \\
n_5(t) &= \zeta\frac{2\rho L_{03}\dot{\varepsilon}_{11}^2}{(1+\varepsilon_{11})^5}\gamma_1^2 & n_6(t) &= \frac{2Y^{(b)}_{,\theta}}{\sqrt{3}(1+\varepsilon_{11})}\gamma_1
\end{aligned}
\tag{45}
$$

with $\zeta = -1$ at $\tilde{X}_3 = 1$ and $\zeta = 1$ at $\tilde{X}_3 = -1$.

It should be mentioned, from Eqs (43) and (45), that the coefficients a_i, b_i, c_i and n_i are only time dependent and only related to the background solution and to the considered longitudinal wavenumber γ_1. So, clearly, these coefficients are known quantities, prior to any problem solving process applied to the set of equations (42) with boundary conditions (44).

Two options for finding the solutions of Eqs (42) will be explored in the present paper. On the one hand, the system (42) with boundary conditions (44) could be integrated following the frozen coefficient theory. In the classical linear stability analysis ($CLSA$), solutions are searched with the form:

$$
\tilde{\psi}(\tilde{X}_3,t) = \tilde{\psi}^{CLSA}(\tilde{X}_3,t) = Ae^{\eta t}e^{i\tilde{l}\tilde{X}_3} \qquad \tilde{\theta}(\tilde{X}_3,t) = \tilde{\theta}^{CLSA}(\tilde{X}_3,t) = Be^{\eta t}e^{i\tilde{l}\tilde{X}_3}
\tag{46}
$$

where η stands for the perturbation growth rate, $\tilde{l} = lL_{03}$ denotes the non dimensional transversal wavenumber and i is the imaginary unit. This case

falls into the classical linear stability analysis and the equations of [24] are retrieved from system (42), see AppendixC. From Eq.(46) and AppendixC, four complex transversal modes $\tilde{l}$ are computed. As a consequence, both perturbed stream function $\tilde{\psi}$ and perturbed temperature $\tilde{\theta}$ are expressed as linear combinations of complex exponential functions of these transversal modes but remain real (see [24] for more details). The perturbation is growing when a positive growth rate η is found. In the CLSA theory, each perturbation of any mechanical quantities is assumed to have the same growth rate η with the same transversal wavenumbers $\tilde{l}$. In addition, the frozen coefficient theory implies that the time scale inherited from the development of the perturbation must be much smaller than the time scale of the background solution, which means that the ratio $\eta/\dot{\varepsilon}_{11}$ must be much larger than unity. Such time scale separation is sometimes not verified, especially when very large strain rates ($10^4/10^5\ s^{-1}$) are considered. This will be explored in the section dedicated to the results.

On the other hand, the system (42) with boundary conditions (44) can be discretized on the time and space domains so that no assumption needs to be made on the shape and on the time dependency of the two unknowns $\tilde{\psi}$ and $\tilde{\theta}$. This method is an extension of the classical theory. It has not been yet explored in the literature and stands as the main novelty of our contribution; it will be denoted $XLSA$. As already stated, a numerical scheme is needed to solve the coupled system and identify the two unknowns $\tilde{\psi}(\tilde{X}_3, t)$ and $\tilde{\theta}(\tilde{X}_3, t)$ or equivalently $\hat{\psi}(X_3, t)$ and $\hat{\theta}(X_3, t)$. This is the subject of the

forthcoming section.

3. Resolution by a spectral decomposition

The set of equations (42) previously established is composed of partial differential equations with fourth order differentiation with respect to space, and second order differentiation with respect to time. The solution cannot be obtained in closed form and a numerical strategy needs to be developed. In the present work, the dependency of the two unknowns $\tilde{\psi}$ and $\tilde{\theta}$ on the position $\tilde{X}_3$ is expanded into a series of Chebyshev polynomials while the time dependency is solved using a finite difference scheme. Note that in [26], dedicated to the study of multiple necking during the dynamic expansion of tubes, a Galerkin method was selected together with the use of the canonical polynomials of the form $h_n(\tilde{X}_3) = (\tilde{X}_3)^n$.

3.1. Tau method

The Tau spectral method, originally proposed by [22], is selected to solve the system of equations (42) with boundary conditions (44). $\tilde{\psi}$ and $\tilde{\theta}$ are interpolated by using the following series of Chebyshev polynomials on the space domain $[-1, 1]$, i.e. for $\tilde{X}_3$ in $[-1, 1]$:

$$\tilde{\psi}(\tilde{X}_3, t) = \sum_{i=0}^{\infty} q_i(t) T_i(\tilde{X}_3) \tag{47a}$$

$$\tilde{\theta}(\tilde{X}_3, t) = \sum_{i=0}^{\infty} p_i(t) T_i(\tilde{X}_3) \tag{47b}$$

The vector $\mathbf{q} = (q_0\ q_1\ \ldots)$ (resp. $\mathbf{p} = (p_0\ p_1\ \ldots)$) is the spectral representation of $\tilde{\psi}$ (resp. $\tilde{\theta}$). $T_n(\tilde{X}_3)$ denotes the Chebyshev polynomial of the first kind, of degree n:

$$T_n(\tilde{X}_3) = \cos\left(n \arccos(\tilde{X}_3)\right) \text{ with } n \geq 0\,. \tag{48}$$

The following scalar product can be defined:

$$< T_m, T_n >= \int_{-1}^{1} \frac{T_m T_n}{\sqrt{1-X^2}} dX \qquad m, n \geq 0\,. \tag{49}$$

The functions T_n form an orthogonal basis for real functions. Indeed, one has:

$$< T_0, T_0 >= \pi \qquad < T_n, T_n >= \pi/2 \text{ for } n > 0 \qquad < T_m, T_n >= 0 \text{ for } m \neq n \tag{50}$$

More information can be found in any textbook ([3] for example) and some important results are recalled in AppendixA.

The spectral decomposition (47) introduced into Eq. (42a) provides a function, denoted by M, and given by:

$$M(\tilde{X}_3) = \sum_{i=0}^{\infty} \left(\frac{a_1}{L_{03}^2} \frac{d^2 q_i^{(2)}}{dt^2} + a_2 \frac{d^2 q_i}{dt^2} + \frac{a_3}{L_{03}^4} \frac{dq_i^{(4)}}{dt} + \frac{a_4}{L_{03}^2} \frac{dq_i^{(2)}}{dt} + a_5 \frac{dq_i}{dt} + \frac{a_6}{L_{03}^2} q_i^{(2)} + \frac{a_7}{L_{03}} p_i^{(1)} \right) T_i(\tilde{X}_3) \tag{51}$$

where $\mathbf{q^{(m)}}$ denotes the spectral representation of the m-th order spatial derivative $\dfrac{\partial^m \tilde{\psi}}{\partial \tilde{X}_3^m}$ of $\tilde{\psi}$. In AppendixA, it is shown that $\mathbf{q^{(m)}}$ is expressed only

as a function of $\mathbf{q}$ through the spectral derivative matrix denoted by $\mathbf{D_S}$. Similarly, the spectral interpolation (47) used in the temperature evolution law (42b) provides a second function, denoted by H, and expressed as:

$$H(\tilde{X}_3) = \sum_{i=0}^{\infty} \left(\frac{dp_i}{dt} + b_1 p_i + \frac{b_2}{L_{03}} \frac{dq_i^{(1)}}{dt} + \frac{b_3}{L_{03}} q_i^{(1)} \right) T_i(\tilde{X}_3) \tag{52}$$

The order of truncation has not yet been specified so that $\tilde{\psi}$ and $\tilde{\theta}$ are expanded into an infinite series in Eq. (47). We define $\tilde{\psi}_N$ (respectively $\tilde{\theta}_{N-1}$), the truncated expansion to the order N (respectively $N-1$) of $\tilde{\psi}$ (respectively $\tilde{\theta}$). $\tilde{\psi}_N$ is a N-th order polynomial meaning that $\tilde{\psi}_{N,3}$ is a $N-1$-th order polynomial. To maintain consistency with respect to the thermal equation (42b), a difference in the truncation order for the two unknowns is necessary since the order of truncation of $\tilde{\theta}$ has to be the same as $\tilde{\psi}_{,3}$. As a result, $2N+1$ relations are needed to calculate $\mathbf{q} = (q_0\ q_1\ \ldots\ q_N)$ and $\mathbf{p} = (p_0\ p_1\ \ldots\ p_{N-1})$.

The Tau method requires that the residuals M_N and H_N, derived from the truncation of both functions M and H, satisfy the orthogonality condition with respect to each of the Chebyshev polynomials. When M_N is considered, this condition leads to a set of $N-3$ equations :

$$\forall i \in [0, N-4], \quad \frac{a_1}{L_{03}^2} \frac{d^2 q_i^{(2)}}{dt^2} + a_2 \frac{d^2 q_i}{dt^2} + \frac{a_3}{L_{03}^4} \frac{dq_i^{(4)}}{dt} + \frac{a_4}{L_{03}^2} \frac{dq_i^{(2)}}{dt} + a_5 \frac{dq_i}{dt} + \frac{a_6}{L_{03}^2} q_i^{(2)} + \frac{a_7}{L_{03}} p_i^{(1)} = 0 \tag{53}$$

Indeed, Eq. (42a) contains a fourth order derivative term. Thus, the scalar product with polynomials of order less or equal than $N-4$ will be only

retained since $\frac{\partial^4 \tilde{\psi}_N}{\partial \tilde{X}_3^4}$ is a polynomial of degree $N-4$. It should be mentioned that the $N-3$ equations are second order time differential equations including a combination of coefficients originating from the perturbed stream function $\tilde{\psi}$ and the perturbed temperature $\tilde{\theta}$. A strong thermo-mechanical coupling is still existing.

The orthogonality condition between the Chebyshev polynomials and the residual H_N provides a set of N equations :

$$\forall i \in [0, N-1], \qquad \frac{dp_i}{dt} + b_1 p_i + \frac{b_2}{L_{03}} \frac{dq_i^{(1)}}{dt} + \frac{b_3}{L_{03}} q_i^{(1)} = 0 \tag{54}$$

Four additional equations are obtained from the boundary conditions (44) ($\delta T_{31} = 0$ and $\delta T_{33} = 0$ at $\tilde{X}_3 = \pm 1$) (For representative convenience, we imposed for the N^{th} component of the temperature perturbation to be equal

to zero $p_N = 0$):

$$\text{for } \tilde{X}_3 = 1: \quad \sum_{i=0}^{N} \left(\frac{1}{L_{03}^2} \frac{dq_i^{(2)}}{dt} + c_1 \frac{dq_i}{dt} - \gamma_1 c_2 q_i \right) = 0 \tag{55a}$$

$$\text{for } \tilde{X}_3 = -1: \quad \sum_{i=0}^{N} (-1)^i \left(\frac{1}{L_{03}^2} \frac{dq_i^{(2)}}{dt} + c_1 \frac{dq_i}{dt} - \gamma_1 c_2 q_i \right) = 0 \tag{55b}$$

$$\text{for } \tilde{X}_3 = 1: \quad \sum_{i=0}^{N} \left(\frac{n_1}{L_{03}} \frac{d^2 q_i^{(1)}}{dt^2} + \frac{n_2}{L_{03}^3} \frac{dq_i^{(3)}}{dt} + \frac{n_3}{L_{03}} \frac{dq_i^{(1)}}{dt} + \frac{n_4}{L_{03}} q_i^{(1)} + n_5 q_i + n_6 p_i \right) = 0 \tag{55c}$$

$$\text{for } \tilde{X}_3 = -1: \quad \sum_{i=0}^{N} (-1)^i \left(\frac{n_1}{L_{03}} \frac{d^2 q_i^{(1)}}{dt^2} + \frac{n_2}{L_{03}^3} \frac{dq_i^{(3)}}{dt} + \frac{n_3}{L_{03}} \frac{dq_i^{(1)}}{dt} + \frac{n_4}{L_{03}} q_i^{(1)} + n_5 q_i + n_6 p_i \right) = 0 \tag{55d}$$

To obtain Eqs (55), we have used the values of the Chebyshev polynomials at $\tilde{X}_3 = \pm 1$: $T_n(1) = 1$ et $T_n(-1) = (-1)^n$.

3.2. Time integration

Equations (53), (54) and (55) form a system of $2N+1$ ordinary differential equations whose solutions are the spectral coefficients q_i and p_i. Since these coefficients are time dependent, initial conditions for ($\mathbf{q}(t_0 = 0)$, $\dot{\mathbf{q}}(t_0 = 0)$ and $\mathbf{p}(t_0 = 0)$) are also needed. Similarly to computations for thermo-

mechanical coupled problems, a staggered grid is adopted. The equations are discretized and time derivatives are approximated by a finite difference scheme. The discretized equations are provided in AppendixB.

4. Results

In the present work, the geometrical configuration is fixed. A plate of half-dimensions $L_{01} = 1\ m$ and $L_{03} = 1\ cm$ is subjected to dynamic loading. The nominal strain rate is $\dot{\varepsilon}_{11} = V_{01}/L_{01}$. The mass density is $\rho = 5000\ kg.m^{-3}$. Initially, the accumulated plastic strain is $\varepsilon_p(t = 0) = 0$. The flow stress, expressed in its general form by Eq.(4), is given in this section by:

$$Y = K\left(\varepsilon_p + \varepsilon_i\right)^n \left(\frac{\dot{\varepsilon}_p}{\dot{\varepsilon}_0}\right)^m \left(\frac{\theta}{\theta_0}\right)^{-\beta} \tag{56}$$

where n is the strain hardening coefficient, m the strain rate sensitivity parameter, β the thermal softening coefficient. K and $\dot{\varepsilon}_0$ are material parameters. θ_0 stands for a reference temperature and ε_i can be viewed as a pre-strain and will be named strain parameter in the following. In this section, all results are obtained with fixed values for $K = 1\ GPa$, $n = 0.2$, $\dot{\varepsilon}_0 = 1\ s^{-1}$ and $\theta_0 = 293\ K$.

In a first part, we will focus on a material with only strain hardening ($m = \beta = 0$ in Eq. (56)). The effects of the nominal strain rate, the strain parameter ε_i and initial conditions will be assessed. The latter point is of

particular interest within the context of our proposed approach. Indeed, by constrast with the classical linear stability analysis (*e.g.* [25], [24] or [20] for the plain strain case), our model provides an intrinsic time evolution of a given perturbation, so that the influence of the initial conditions needs to be explored. In the second part, the material is thermo-viscoplastic and the role of viscosity and thermal softening is addressed.

The evolution of the perturbation and the effect of the initial conditions are studied using the spectral method specified in Section 3. Time integration is obtained with the finite difference scheme detailed in AppendixB. In the following, we have adopted $N = 20$ Chebyshev polynomials and a integration timestep of 0.02 μs (resp. 0.002 μs) for a nominal strain rate of 1000 s^{-1} (resp. 10000 s^{-1}). A convergence study (not presented here) has shown that a larger truncation order N and a smaller integration timestep would give identical results.

4.1. Rate insensitive materials

In this section, the material is rate insensitive and thermal softening is ignored. Therefore, the flow stress is obtained from Eq.(56) with $m = 0$ and $\beta = 0$:

$$Y = K\left(\varepsilon_p + \varepsilon_i\right)^n \tag{57}$$

For this type of material, the onset of the plastic instability is often determined using the Considère criterion (see [4]). Based on experimental obser-

vations, instabilities start to appear when the traction force on the surfaces $X_1 \pm L_{01}$ is maximum. This criterion has been retrieved using the CLSA (see [25] or [19]) as positive growth rates are found around the maximum force. With the material constitutive law considered here (see Eq.57), the expression for the force F existing at the surfaces $X_1 = \pm L_{01}$ (by unit length in the transversal direction X_2) under quasi-static plain strain conditions is:

$$F = 4K/\sqrt{3}\,(\varepsilon_p + \varepsilon_i)^n\, L_{03} \exp(-\sqrt{3}\varepsilon_p/2) \tag{58}$$

The maximum of the traction force, denoted F_{max} is defined by the condition $\frac{\partial F}{\partial \varepsilon_p}(\varepsilon_c) = 0$ where ε_c is referred to as the Considère strain. From Eq. (58), we obtain $\varepsilon_c = \frac{2n}{\sqrt{3}} - \varepsilon_i$. If $\varepsilon_i > \frac{2n}{\sqrt{3}}$ then F is monotonically decreasing as ε_p increases. Thus, the flow is initially unstable. On the contrary, if $\varepsilon_i < \frac{2n}{\sqrt{3}}$ then F grows until $\varepsilon_p = \varepsilon_c$ where F reaches its maximum F_{max} then decreases as ε_p increases : the flow is stable until $\varepsilon_p = \frac{2n}{\sqrt{3}} - \varepsilon_i$.

Fig. 2 represents the evolution of the force registered at $X_1 = \pm L_{01}$, normalized by F_{max} as a function of the accumulated plastic strain ε_p for various values of ε_i. With $n = 0.2$, the Considere strain is $\varepsilon_c = 0.23 - \varepsilon_i$ meaning that the flow becomes unstable when the plastic strain ε_p overcomes $0.23 - \varepsilon_i$. One observes, from Fig. 2, that for $\varepsilon_i = 0$ and $\varepsilon_i = 0.1$, the maximum force occurs after some plastic straining, so that the flow is initially stable. On the contrary, for $\varepsilon_i = 0.4$, the normalized force is a decreasing function of the plastic strain, and is lower than one (maximum force is already

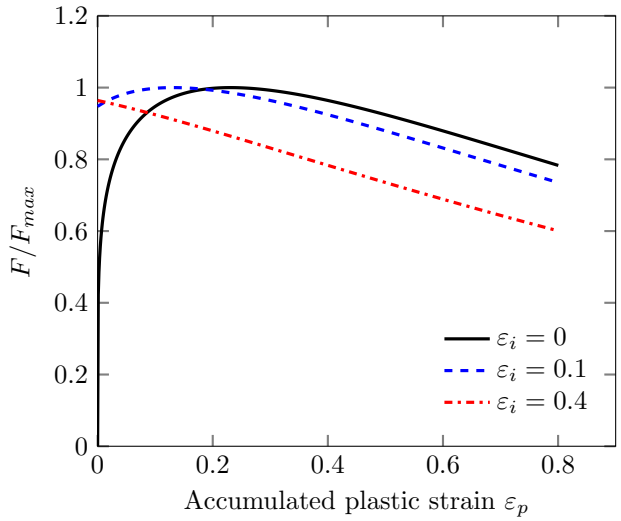

Figure 2: Normalized force F/F_{max} registered at $X_1 = \pm L_{01}$ by unit length in the transversal direction X_2, as a function of the accumulated plastic strain ε_p. Plain strain conditions are prescribed. Three values of the strain parameter ε_i are considered. The value of the strain parameter ε_i for the material flow law (57) will determine whether the flow is initially unstable or not. If $2n/\sqrt{3} - \varepsilon_i < 0$ (resp. $2n/\sqrt{3} - \varepsilon_i > 0$) then the flow is unstable (resp. stable)

overcome) meaning that the flow is initially unstable.

4.1.1. Unstable flow case

We first consider the case where $\varepsilon_i = 0.4$ (the flow is initially unstable). Two values of the velocity applied to the surface $X_1 = \pm L_{01}$ are considered: $V_{01} = 1\,000\ m.s^{-1}$ and $V_{01} = 10\,000\ m.s^{-1}$, leading to nominal strain rates $\dot{\varepsilon}_{11} = 1\,000\ s^{-1}$ and $\dot{\varepsilon}_{11} = 10\,000\ s^{-1}$, respectively.

Before presenting results based on the proposed model, we explore the predictions of the classical linear stability analysis. The growth rate provided by the CLSA at $t = 0$ is denoted η_0. Figure 3 presents the evolution of the

normalized growth rate $\eta_0/\dot{\varepsilon}_{11}$ as a function of the wavenumber $\gamma_1 = i_1\pi/L_{01}$ for $V_{01} = 1000\ m.s^{-1}$ *i.e.* $\dot{\varepsilon}_{11} = 1000\ s^{-1}$ (Figure 3a) and $V_{01} = 10000\ m.s^{-1}$ *i.e.* $\dot{\varepsilon}_{11} = 10000\ s^{-1}$ (Figure 3b). At the lowest velocity, Figure 3a reveals that $\eta_0/\dot{\varepsilon}_{11} > 1$ for most of the wavenumbers, meaning that the frozen coefficient theory is supposed to be relevant for the set of material parameters considered here. Note that a critical wavenumber γ_1^c (perturbation having the maximum growth rate) can be identified, see vertical dashed line in Fig. 3a: $\gamma_1^c = 23\pi/L_{01}$ with corresponding growth rate $\eta_0^c = 13517\ s^{-1}$ and normalized growth rate $\eta_0^c/\dot{\varepsilon}_{11} = 13.5$. For the largest nominal strain rate, Fig. 3b reveals the same critical wavenumber $\gamma_1^c = 23\pi/L_{01}$ with a corresponding growth rate $\eta_0^c = 6651\ s^{-1}$ and a very limited relative growth rate $\eta_0^c/\dot{\varepsilon}_{11} = 0.66$. Therefore $\eta_0/\dot{\varepsilon}_{11} < 1$ for all the wavenumbers implying that the time scale separation in terms of evolution rate between the fundamental solution and the perturbation is no more satisfied. For this high strain rate case, the frozen coefficient theory thus may be questionable. The new approach is developed to tackle this situation.

With the proposed approach, the evolution law for the perturbation provided in Eq. (42a) is a second order differential equation. So initial conditions in terms of $\tilde{\psi}(\tilde{X}_3, t = 0)$ and $\dot{\tilde{\psi}}(\tilde{X}_3, t = 0)$ need to be provided. From the previous section, $\tilde{\psi}(\tilde{X}_3, t = 0)$ and $\dot{\tilde{\psi}}(\tilde{X}_3, t = 0)$ are representative of the deviations of the position and of the velocity from the homogeneous solution. In this work, four initial conditions (IC1 to IC4) defined in Table 1 are tested to rationalize their role on the early and late evolution stages of a

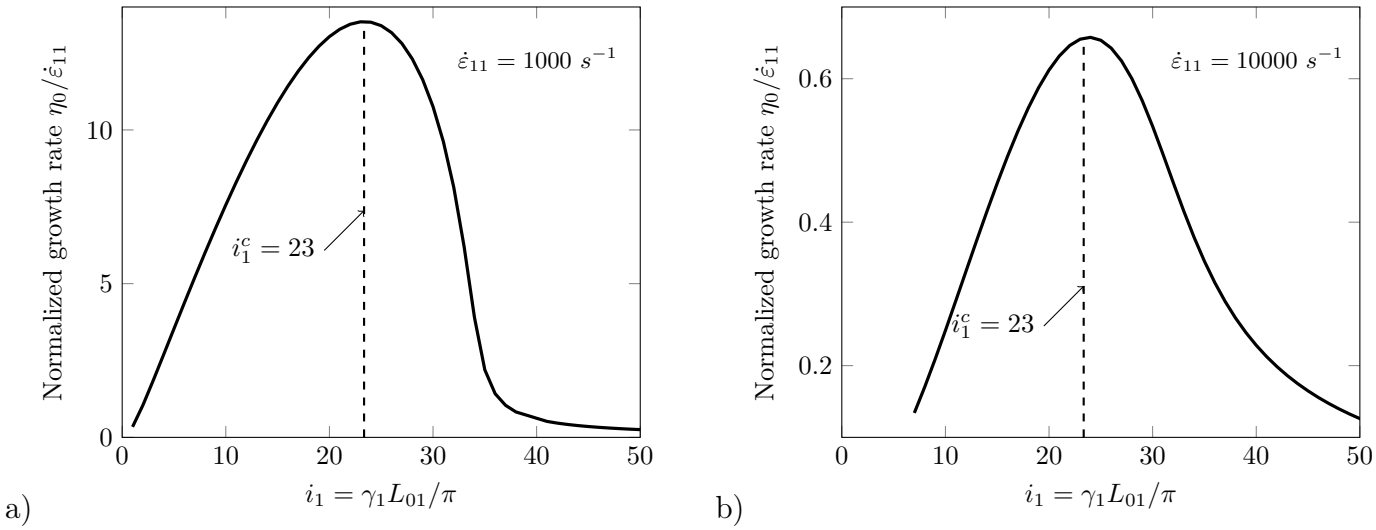

Figure 3: Normalized growth rate determined by the Classical LSA at $t = 0$ (accumulated plastic strain $\varepsilon_p = 0$) as a function of the wavenumber index i_1 ($\gamma_1 = \frac{i_1 \pi}{L_{01}}$) for a) $V_{01} = 1000\ m.s^{-1}$ i.e. $\dot{\varepsilon}_{11} = 1000\ s^{-1}$ and b) $V_{01} = 10000\ m.s^{-1}$ i.e. $\dot{\varepsilon}_{11} = 10000\ s^{-1}$. The material flow stress is given by Eq.(57) with $K = 1GPa$, $n = 0.2$. The strain parameter $\varepsilon_i = 0.4$ (the flow is initially unstable).

perturbation.

	$\tilde{\psi}(\tilde{X}_3, t = 0)$	$\dot{\tilde{\psi}}(\tilde{X}_3, t = 0)$
$IC1$	$A_0 \tilde{\psi}^{CLSA}(\tilde{X}_3, t = 0)$	$A_0 \eta_0 \tilde{\psi}^{CLSA}(\tilde{X}_3, t = 0)$
$IC2$	$A_0 \tilde{\psi}^{CLSA}(\tilde{X}_3, t = 0)$	$4 A_0 \eta_0 \tilde{\psi}^{CLSA}(\tilde{X}_3, t = 0)$
$IC3$	$A_0 \tilde{\psi}^{CLSA}(\tilde{X}_3, t = 0)$	0
$IC4$	$A_0 \sin(\omega \tilde{X}_3)$	$\dot{\varepsilon}_{11} A_0 \sin(\omega \tilde{X}_3)$

Table 1: Definition of initial conditions. IC1, IC2 and IC3 are derived from the classical linear stability analysis, see Eq. (59). A_0 is an amplitude factor which does not influence the results presented in the paper, so that no specific value needs to be specified. IC4 is a periodic function with $\omega = 5\pi/2$. Two values of the nominal strain rate are tested: $\dot{\varepsilon}_{11} = 1\,000 s^{-1}, 10\,000 s^{-1}$.

IC1, IC2, IC3 are based on the solution obtained from the classical linear

stability analysis. Indeed, $\tilde{\psi}(\tilde{X}_3, t=0) = A_0\tilde{\psi}^{CLSA}(\tilde{X}_3, t=0)$ and $\dot{\tilde{\psi}}(\tilde{X}_3, t=0) = \alpha A_0\eta_0\tilde{\psi}^{CLSA}(\tilde{X}_3, t=0)$ where $\alpha = 1$ for IC1, $\alpha = 4$ for IC2, $\alpha = 0$ for IC3 and A_0 is an amplitude factor. The solution $\tilde{\psi}^{CLSA}(\tilde{X}_3, t=0)$ and $\dot{\tilde{\psi}}^{CLSA}(\tilde{X}_3, t=0)$ are written as:

$$\begin{aligned}\tilde{\psi}^{CLSA}(\tilde{X}_3, t_0=0) &= \exp\left(i\tilde{l}_0\tilde{X}_3\right)\\ \dot{\tilde{\psi}}^{CLSA}(\tilde{X}_3, t_0=0) &= \eta_0\exp\left(i\tilde{l}_0\tilde{X}_3\right)\end{aligned} \tag{59}$$

where $\tilde{l}_0$ and η_0 are determined according to the work of [24], see AppendixC for more details. Note that A_0 has no effect on the evolution of the perturbation, since the CLSA or the new approach XLSA are linear perturbation analyses. Nevertheless, A_0 is chosen so as to be physically relevant of a small perturbation.

The initial conditions IC1, IC2 and IC3 are illustrated in Fig. 4 which shows the evolution of $\tilde{\psi}(\tilde{X}_3, t=0)$ within the plate for two applied velocities and wavenumbers. $\gamma_1 = \frac{23\pi}{L_{01}}$ corresponds to the critical wavenumber revealed in Fig. 3. A second wavenumber $\gamma_1 = \frac{35\pi}{L_{01}}$ is also considered having a much lower growth rate at $t = 0$, see Fig. 3. Owing to the value of transversal wavenumber $\tilde{l}_0$ predicted by the CLSA, it appears from Fig. 4 that $\tilde{\psi}^{CLSA}(\tilde{X}_3, t=0)$ is almost linear. In order to test a more general initial condition, an additional case, denoted by IC4, is considered with $\tilde{\psi}(\tilde{X}_3, t=0) = A_0\sin(\omega\tilde{X}_3)$ and $\dot{\tilde{\psi}}(\tilde{X}_3, t=0) = \dot{\varepsilon}_{11}A_0\sin(\omega\tilde{X}_3)$ with $\omega = 5\pi/2$. Thus IC4 is not related to the CLSA.

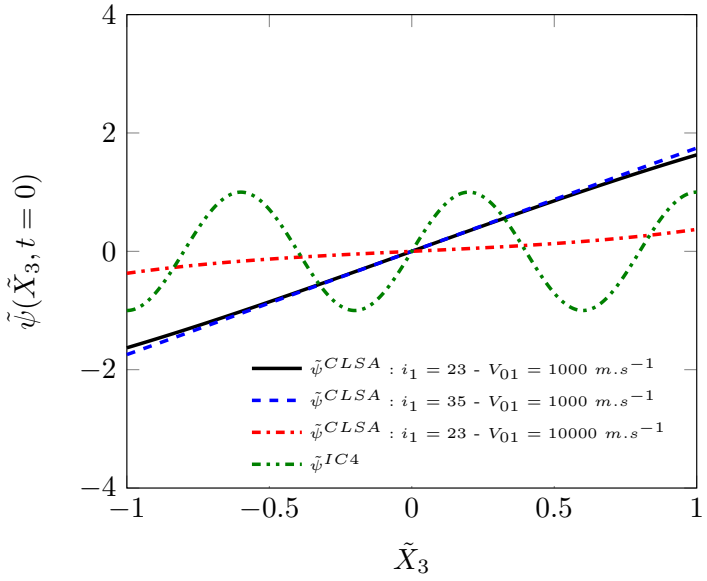

Figure 4: Through thickness dependency of the initial conditions $\tilde{\psi}(\tilde{X}_3, t = 0)$. Results are presented for two different wavenumbers $\gamma_1 = i_1\pi/L_{01}$ (with $i_1 = 23$ and $i_1 = 35$) and two applied velocities $V_{01} = 1000\ m/s$ or $10000\ m/s$. $\tilde{\psi}^{CLSA}$ is derived from results of the classical linear stability analysis. The initial condition $\tilde{\psi}^{IC4}$ is not linked to the CLSA and has a sinusoidal shape, so as to be highly different from the three others (see Table 1).

For comparison purpose, the instantaneous growth rate of the perturbation $\eta(t)$ at the free surface ($\tilde{X}_3 = 1$) is defined as:

$$\eta(t) = \frac{\dot{\tilde{\psi}}(\tilde{X}_3 = 1, t)}{\tilde{\psi}(\tilde{X}_3 = 1, t)} \tag{60}$$

It is compared to the growth rate of the perturbation predicted by the CLSA.

The normalized growth rate $\eta/\dot{\varepsilon}_{11}$ obtained adopting the initial conditions IC1 to IC4 is computed at each step of the deformation process from $\varepsilon_{11} = V_{01}t/L_{01} = 0$ to $\varepsilon_{11} = 1$. Results are presented in Fig. 5 for two

velocities, $V_{01} = 1\,000,\ 10\,000 m/s$ and two wavenumbers : $\gamma_1 = 23\pi/L_{01}$ and $\gamma_1 = 35\pi/L_{01}$. From Fig. 5, it is observed that for all tested cases, the normalized growth rate of the perturbation is highly dependent on the initial conditions (*i.e.* the shape of the initial perturbation) in the early stages of the deformation process but is almost independent in the late stage. This is particularly marked for the lower velocity case ($V_{01} = 1\,000 m/s$, see Fig. 5a-b), where the results obtained from our model based on the four initial conditions coincide after $t \simeq 180\ \mu s$ (nominal strain $\varepsilon_{11} = 0.18$). Fig. 5 a) and b) reveal that in the late stages, the normalized growth rate obtained from our new model is close to the predictions of the classical linear stability approach. It confirms that the CLSA based on the frozen coefficient theory with definitions (46) is relevant in the case where the perturbation has a growth rate larger than the nominal strain rate $\dot{\varepsilon}_{11}$. By comparing results of Fig. 5 a and b, it is also seen that at late stage of the deformation process, the growth rate of the perturbation with wavenumber $\gamma_1 = 23\pi/L_{01}$ (Fig. 5a) is smaller than the growth rate of the perturbation with wavenumber $\gamma_1 = 35\pi/L_{01}$ (Fig. 5b). This confirms that the most unstable perturbation mode is evolving with time. As deformation proceeds, shorter wavelength modes develop faster. This has been already reported in the literature using the classical linear stability analysis, see for instance [25]. The trend is confirmed by our model without using the frozen coefficient theory.

For the larger velocity leading to a nominal strain rate of $\dot{\varepsilon}_{11} = 10000\ s^{-1}$,

see Figs. 5 c) and d), it is clearly seen that even for large deformation, the predictions of the classical approach are not fully retrieved. Indeed, even for $t = 0.1\ ms$ (*i.e.* $\varepsilon_{11} = 1$), the predictions based on the four initial conditions IC1 to IC4 are still different (5% difference between predictions, see Fig. 5 c)). The normalized growth rate given by the Classical LSA is lower when compared to other predictions. One should mention however that the linear stability analysis based on the frozen coefficient theory provides a good approximate for the growth rate of the perturbation in the very late stages. In fact, differences are at most 5% between the growth rate given by the classical theory and the new approach.

4.1.2. Stable flow case

The situation depicted above is valid for a configuration where the flow is initially unstable. One of the main interests of the proposed work is that the new approach is able to tackle perturbation evolution even when the flow is supposed to be stable.

In the literature dedicated to CLSA, positive growth rates are searched. The evolution of the perturbation during the stable phase of the plastic flow is not addressed. Once positive growth rates are found (at $t = t_i$), the amplitude $A(t)$ estimated using the classical approach is obtained from the integration of the instantaneous growth rate provided at each time step (see

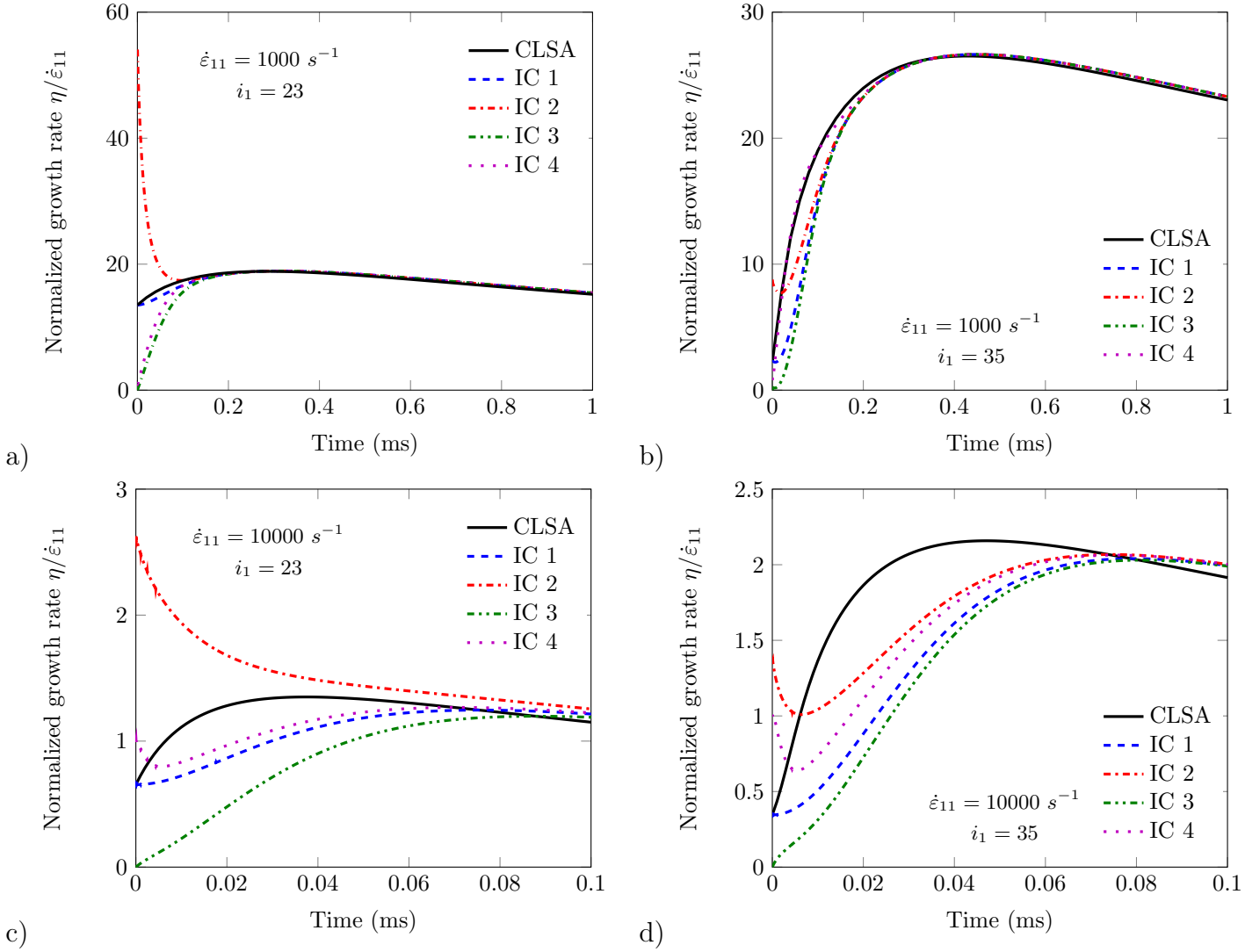

Figure 5: Time evolution of the normalized growth rate $\eta/\dot{\varepsilon}_{11}$ of a perturbation with wavenumber $\gamma_1 = i_1\pi/L_{01}$ a) $i_1 = 23$, b) $i_1 = 35$; the nominal strain rate is $\dot{\varepsilon}_{11} = 1000\ s^{-1}$. c) $i_1 = 23$, d) $i_1 = 35$; the nominal strain rate is larger : $\dot{\varepsilon}_{11} = 10000\ s^{-1}$. The growth rate is defined in Eq.(60). The initial conditions are defined in Table 1 and represented in Fig.(4). The flow stress is given by Eq. (57) with $K = 1GPa$ and $n = 0.2$. The strain parameter is $\varepsilon_i = 0.4$.

[9], [31], [6] or [38]) as follows :

$$A(t) = A_0 \exp(\int_{t_i}^{t} \eta(\tau) d\tau) \tag{61}$$

With the present approach, the perturbation is naturally time evolving as solution of Eq. (42a).

Since at $t = 0$ the flow is stable, the classical approach does not provide a positive growth rate for the perturbation under the form given by Eq.(59). Therefore, the initialization IC1 to IC3 used in the previous configurations is no more effective. New initial conditions (IC5 and IC6) are therefore proposed, see Table (2). For both IC5 and IC6, $\tilde{\psi}(\tilde{X}_3, t = 0)$ is a linear function with respect to the through thickness variable $\tilde{X}_3$, a choice similar to initial conditions presented in Fig. 4. As already mentioned, the amplitude coefficient A_0 has no influence on the relative evolution (principle of linear stability analysis). The difference between IC5 and IC6 stands in the definition of the rate $\dot{\tilde{\psi}}(\tilde{X}_3, t_0 = 0)$. It has a zero value in IC5, while it varies in a linear manner inside the thickness for the initial condition IC6. In addition, we adopt $B_0/A_0 = 20\dot{\varepsilon}_{11}$ ($= 20000s^{-1}$ for a nominal strain rate $1000s^{-1}$) to specify IC6. With such a ratio, we consider that the time scale separation between the background solution and the perturbation is satisfied.

To illustrate the main result of the present approach, we keep all parameters of the reference configuration of Section 4.1.1 unchanged except the strain parameter which is now reduced to $\varepsilon_i = 0.1$. At a nominal strain rate

Table 2: Definition of the initial conditions for the case of rate insensitive material when the flow is stable at $t = 0$.

	$\tilde{\psi}(\tilde{X}_3, t = 0)$	$\dot{\tilde{\psi}}(\tilde{X}_3, t = 0)$
$IC5$	$A_0\tilde{X}_3$	0
$IC6$	$A_0\tilde{X}_3$	$B_0\tilde{X}_3$

$B_0/A_0 = 20\dot{\varepsilon}_{11}$

of $1000s^{-1}$, the flow remains stable until $t < 119\ \mu s$.

Firstly, the shape of the normalized stream function evaluated at the free surface $\tilde{X}_3 = 1$ and defined by :

$$\frac{\delta\psi(X_1, \tilde{X}_3 = 1, t)}{A_0} = \frac{\tilde{\psi}(\tilde{X}_3 = 1, t)}{A_0}\sin(\gamma_1 X_1) \tag{62}$$

is plotted as a function of the normalized coordinate $\gamma_1 X_1$ in Fig.6. The comparative evolution is presented for different times and for two wavenumbers $\gamma_1 = 23\pi/L_{01}$ (Fig.6a) and $\gamma_1 = 85\pi/L_{01}$ (Fig.6b). Initial condition IC5 has been adopted. For sake of brevity, results with initial condition IC6 are not presented here since trends are similar. In Figs 6a) and b), the shape of the normalized stream function at $t = 0$ corresponds to the adopted initialization so that the perturbation for both wavenumbers coincides initially. For $\gamma_1 = 23\pi/L_{01}$, at $t = 70\ \mu s$ *i.e.* an accumulated plastic strain $\varepsilon_p = 0.08$, it is seen that the amplitude is reduced. Therefore, with the present approach, we clearly observe that before the Considère criterion is met, a stable flow is associated with a damping of the perturbation. Later at $t = 300\ \mu s$ or

$\varepsilon_p = 0.30$, the instability development becomes significant and the amplitude is six times the initial amplitude. For $\gamma_1 = 85\pi/L_{01}$, the duration of the phase where the amplitude is smaller than the initial one is increased. Indeed, after $t = 200\ \mu s$ or $\varepsilon_p = 0.21$ (a plastic strain greater than the Considère strain), the amplitude of the perturbation is still smaller than the one at $t = 0$. Only, at large deformation, this mode of perturbation becomes highly unstable. As illustrated in Fig. 6b), the associated normalized amplitude at $t = 600\ \mu s$ or $\varepsilon_p = 0.54$ is seven times the initial one. As a consequence, one observes that for both modes of perturbation, prior to Considère, the amplitude of the perturbation evolves strongly (damping of the perturbation). Such an evolution is not yet adressed by the classical linear stability analysis, *i.e.* by using relationship (61).

The results of Fig. 6 are rationalized in a different way by considering the amplitude of the normalized stream function at the free surface $\tilde{X}_3 = 1$:

$$\mathrm{A}_{\delta\psi} = \frac{|\tilde{\psi}(\tilde{X}_3 = 1, t)|}{|\tilde{\psi}(\tilde{X}_3 = 1, t = 0)|} \tag{63}$$

The time evolution of the amplitude $\mathrm{A}_{\delta\psi}$ is presented in Fig.7 a) for the wavenumber $\gamma_1 = 23\pi/L_{01}$ and in Fig.7 b) for the wavenumber $\gamma_1 = 85\pi/L_{01}$. The predictions of the model based on the two different initial conditions IC5 and IC6 are considered as well as the estimate obtained from the CLSA approach given by Eq.(61). For t in the interval where the Considère criterion

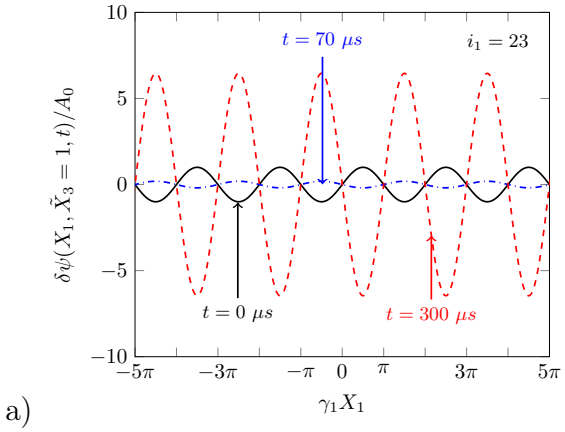

a)

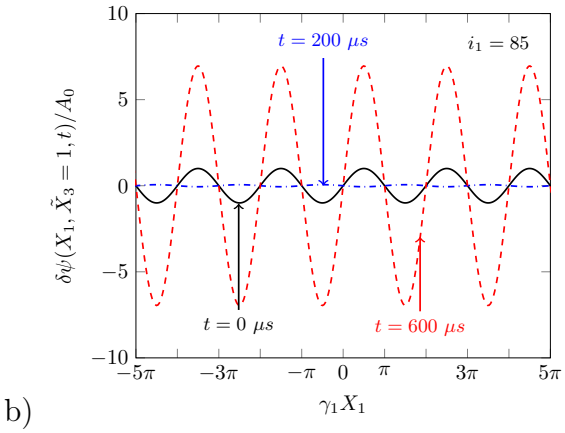

b)

Figure 6: Shape of the stream function $\delta\psi$ as a function of the normalized longitudinal coordinate $\gamma_1 X_1$ for two wavenumbers at different times a) $\gamma_1 = 23\pi/L_{01}$ and $t = 0\mu s$, $t = 70\mu s$ and $t = 300\mu s$. b) $\gamma_1 = 85\pi/L_{01}$ and $t = 0\mu s$, $t = 200\mu s$ and $t = 600\mu s$. The stream function is evaluated at the free surface $\tilde{X}_3 = 1$. The nominal strain rate is $\dot{\varepsilon}_{11} = 1000\ s^{-1}$. The flow stress is given by Eq. (57) with $K = 1GPa$, $n = 0.2$. The strain parameter is $\varepsilon_i = 0.1$. Initial condition $IC5$ is adopted as defined in Table 2.

.

is not fulfilled, the amplitude evaluated by the CLSA approach is not calculated as no positive growth rates are found. For $\gamma_1 = 23\pi/L_{01}$, it is revealed that regardless the initial conditions (IC5 or IC6), the new approach shows

that the perturbation is stabilized first. Indeed, in the range $[0 : 150\ \mu s]$, the amplitude is lower than its initial value while for $t > 150\mu s$, the amplitude grows rapidly. Note that $t = 150\ \mu s$ (or $\varepsilon_p = 0.16$) corresponds closely to the time where the flow becomes highly unstable and therefore where the classical approach captures positive growth rates (the Considère strain is attained at $t = 119\ \mu s$) For the wavenumber $\gamma_1 = 85\pi/L_{01}$, as observed in Fig. 7 b), the time where the perturbation amplitude increases rapidly is larger than $t = 500\mu s$. For $t < 500\mu s$, the amplitude of the perturbation is fluctuating but remains limited, below the amplitude at $t = 0$. This situation pertains during a certain time interval even when the flow is unstable in the sense of the Considère criterion. In more details, the oscillating stage can lead to a perturbation with vanishing amplitude at some particular time. For $\gamma_1 = 23\pi/L_{01}$ the corresponding time depends strongly on the initial conditions as the perturbation vanishes at $\tau_I = 61\ \mu s$ for $IC5$ while it vanishes at $\tau_{II} = 97\ \mu s$ for $IC6$ (see vertical dashed lines on Fig.7 a). For $\gamma_1 = 85\pi/L_{01}$, such feature is observed four times on Fig.7 b); the effect of initial conditions being less visible. The perturbation vanishes for the last time at $\tau_{III} = 324\ \mu s$. An important outcome of the new approach is the capability to evaluate the amplitude change prior to the Considère strain. It is observed that the phase where a rapid growth for the perturbation is triggered occurs at around the same time for the CLSA and XLSA approaches. Nevertheless, with the present model, the development of the perturbation is also captured at the early stage of the deformation. It is also

seen that for both wavenumbers, the influence of the initial perturbation rate $\dot{\tilde{\psi}}(\tilde{X}_3, t_0 = 0)$ vanishes in the late stages. So, Fig. 7 also shows that the effect of the initial conditions is visible in the early stage of the deformation. It has been checked also that, as the nominal strain rate increases, the difference between the XLSA and CLSA is increased in a similar way as presented in Section 4.1.1.

Time evolution of the normalized growth rate of the perturbation is presented in Fig.8 for the two wavenumbers $\gamma_1 = 23\pi/L_{01}$ and $\gamma_1 = 85\pi/L_{01}$. We have seen in Fig.7 has revealed that the amplitude of the perturbation $\tilde{\psi}(\tilde{X}_3 = 1, t)$ can be close to zero (even zero) at some particular times. As a consequence, with $\dot{\tilde{\psi}}(\tilde{X}_3 = 1, t)$ which is bounded, the relative growth rate η defined in Eq. (60) can reach very large values (infinite in theory for a zero amplitude). To avoid such singular situation (identified by vertical dashed lines at times τ_I, τ_{II} and τ_{III} on Fig. 7 a) and b), we have chosen in Fig. 8 to present the time evolution of η in a time interval where the amplitude of $\tilde{\psi}(\tilde{X}_3 = 1, t)$ remains strictly positive ($t > \tau_I = 61\ \mu s$ (resp. $t > \tau_{II} = 97\ \mu s$) for $\gamma_1 = 23\pi/L_{01}$ with initial condition $IC5$ (resp. $IC6$) and $t > \tau_{III} = 324\ \mu s$ for $\gamma_1 = 85\pi/L_{01}$.) It is seen that the predictions of the new model are in close agreement with the results obtained from the classical approach at the large deformation stage. In the early stage of the process, the effect of the initial conditions is clearly highlighted. The CLSA has not yet studied the time evolution prior to the Considère strain or even closely after the maximum force is reached. For the wavenumber $\gamma_1 = 23\pi/L_{01}$, after

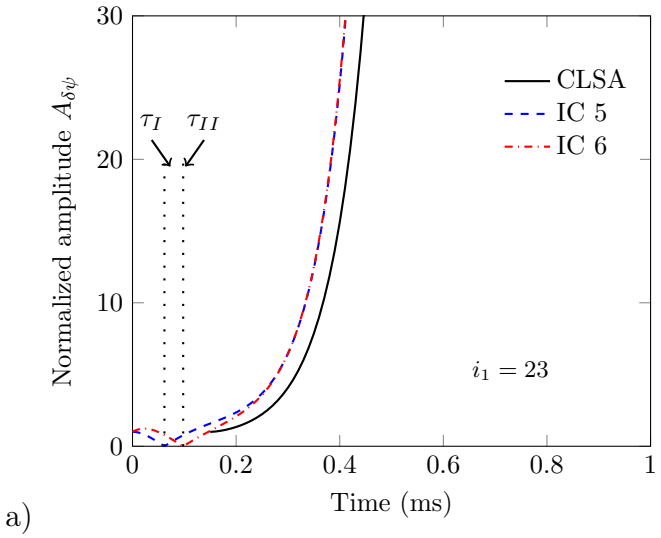

a)

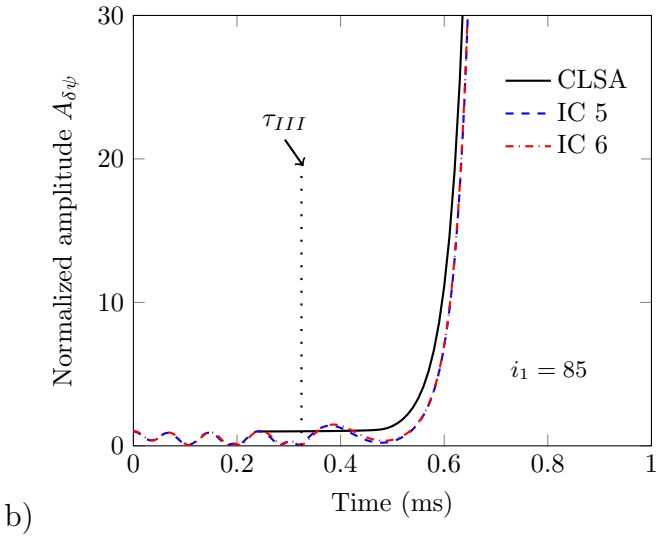

b)

Figure 7: Normalized amplitude $A_{\delta\psi}$ of a perturbation with wavenumber a) $\gamma_1 = 23\pi/L_{01}$ b) $\gamma_1 = 85\pi/L_{01}$. The nominal strain rate is $\dot{\varepsilon}_{11} = 1000\ s^{-1}$. The flow stress is given by Eq.(57) with $K = 1GPa$ and $n = 0.2$. The strain parameter is $\varepsilon_i = 0.1$. Initial conditions IC5 and IC6 are adopted and defined in Table 2. Amplitude evaluated based on the classical LSA Eq.(61) is also added.

the Considère strain, growth rates are positive for both the CLSA and our new approach. For the wavenumber $\gamma_1 = 85\pi/L_{01}$, it is also observed that while the Considère strain is overcome, negative growth rates are captured by the new approach for the two initial conditions. By construction, with CLSA, when the flow is unstable, positive growth rate is captured. Clearly, we have observed the strong influence of the initial conditions with our new approach in the early stage of the deformation for moderate nominal strain rate.

4.2. Case of (thermo)-viscoplastic material

4.2.1. Viscoplastic material

In this section, the material is rate sensitive without thermal softening ($\beta = 0$ in Eq. 56). The flow stress is of the form :

$$Y = K\left(\varepsilon_p + \varepsilon_i\right)^n \left(\frac{\dot{\varepsilon}_p}{\dot{\varepsilon}_0}\right)^m \tag{64}$$

with $K = 1\ GPa$, $n = 0.2$, $\dot{\varepsilon}_0 = 1\ s^{-1}$. The strain parameter is $\varepsilon_i = 0.1$ so that the effect of the rate sensitivity on the perturbation evolution will be explored in the phase where the plastic flow is stable (early in the deformation process). The applied velocity is $V_{01} = 1\,000\ m/s$ leading to a nominal strain rate $\dot{\varepsilon}_{11} = 1000\ s^{-1}$. The influence of the initial conditions will be first discussed for a fixed value of m. Then the effect of the strain rate sensitivity will be studied by adopting various values for the strain rate sensitivity parameter m.

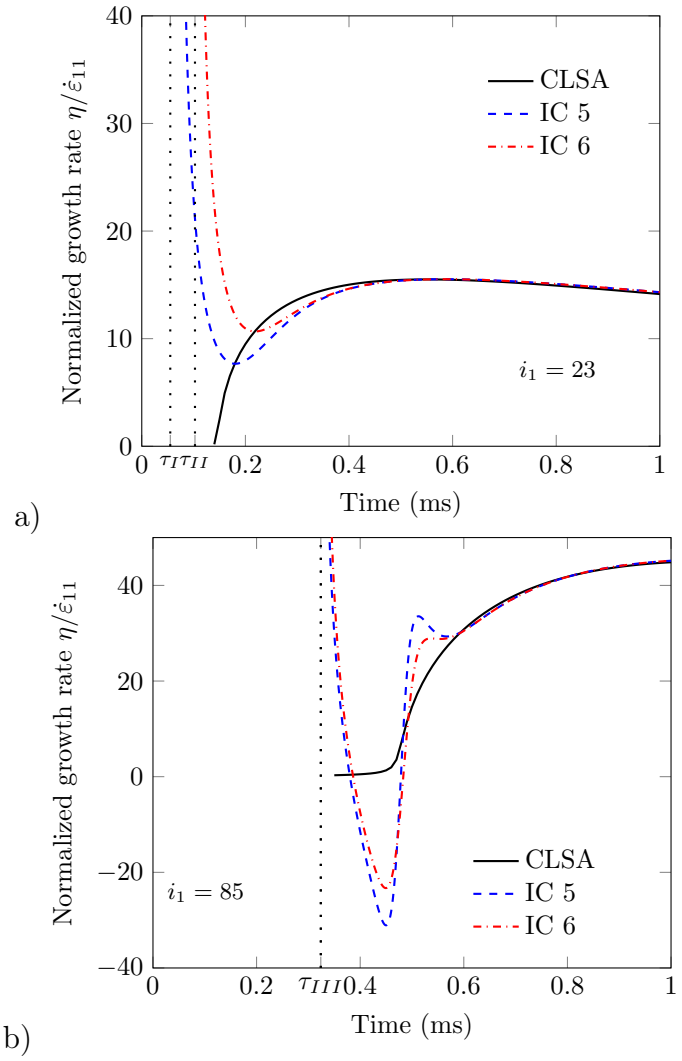

Figure 8: Normalized growth rate $\eta/\dot{\varepsilon}_{11}$ versus time, for a perturbation with wavenumber a) $\gamma_1 = 23\pi/L_{01}$ b) $\gamma_1 = 85\pi/L_{01}$. The nominal strain rate is $\dot{\varepsilon}_{11} = 1000\ s^{-1}$. The flow stress is given by Eq.(57) with $K = 1GPa$, $n = 0.2$. The strain parameter is $\varepsilon_i = 0.1$. Considère strain is attained at $t = 119\ \mu s$. Initial conditions IC5 and IC6 are defined in Table 2. Vertical asymptotes correspond to times $\tau_I = 61\ \mu s$, $\tau_{II} = 97\ \mu s$ and $\tau_{III} = 324\ \mu s$ for which the perturbation has an amplitude equal to 0, see Fig. 7.

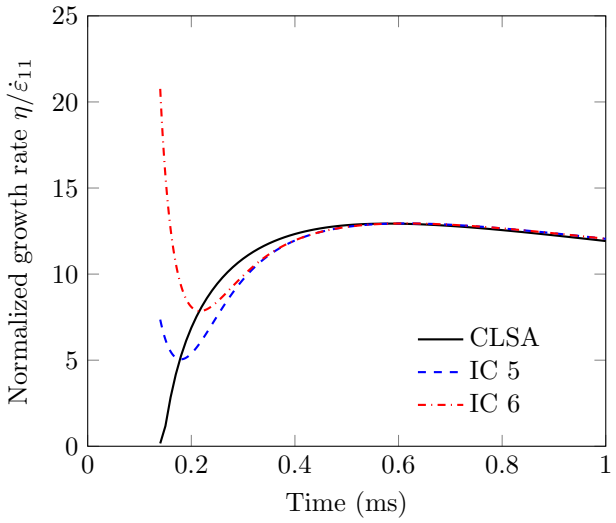

Figure 9: Normalized growth rate $\eta/\dot{\varepsilon}_{11}$ versus time. Effect of initial conditions defined in Table 2. The perturbation wavenumber is $\gamma_1 = 23\pi/L_{01}$. The nominal strain rate of $\dot{\varepsilon}_{11} = 1000\ s^{-1}$. The flow stress is defined by Eq. (64) with a strain rate sensitivity parameter equal to $m = 0.01$ and $\dot{\varepsilon}_0 = 1\ s^{-1}$. Other material parameters are similar to Fig. 8

We first consider the case where the strain rate sensitivity parameter is set to m=0.01. Initial conditions IC5 and IC6 are considered, see Table 2 for their respective definitions. Such a limited strain rate sensitivity is somehow representative of the behavior of metallic alloys under room temperature conditions and moderate strain rate loading. The time evolution of the normalized growth rate $\eta/\dot{\varepsilon}_{11}$ is represented in Fig.9 for a perturbation with wavenumber $\gamma_1 = \frac{23\pi}{L_{01}}$. Again, it is seen that the influence of the initial conditions on the normalized growth rate is important in the early deformation stage but vanishes in the late stage where the growth rate computed by the classical approach is retrieved. The conclusions are similar to the case

of rate insensitive material (see Fig.8). In addition, as for the rate insensitive material, see Section 4.1, the CLSA approach does not provide any solution with a positive growth rate at the beginning of the process. First positive growth rates are found here at around 130 μs (corresponding to an accumulated plastic strain $\varepsilon_p = 0.14 \approx \varepsilon_c$). For larger nominal strain rate $\dot{\varepsilon}_{11} = 10000\ s^{-1}$, it has been checked that differences are still observed when plastic strain is increasing (from $\varepsilon_{11} = 0$ to $\varepsilon_{11} = 1$), as presented in Fig. 5 .

Fig.10 presents the evolution of the normalized growth rate of a perturbation as a function of the wavenumber at a) $t = 490\ \mu s$ (plastic strain $\varepsilon_p = 0.46$) and b) $t = 820\ \mu s$ (plastic strain $\varepsilon_p = 0.69$). Two strain rate sensitivities are considered : $m = 0.01$ and $m = 0.05$. The normalized growth rate computed by the new approach is compared to the growth rate computed by the classical linear stability analysis. At $t = 490\ \mu s$, Fig.10 a) predictions for the normalized growth rate of long wavelength perturbations (small index number i_1) are similar for the CLSA and XLSA models, while some differences are observed for shorter wavelengths (large index number i_1). It is also observed that no difference is revealed between CLSA and XLSA for the presented wavelengths at larger time t. We also observe that viscous effects stabilize the flow as growth rates are damped for all wavenumbers; they particularly affect perturbations with large wavenumbers ($i.e$ short wavelength modes). The perturbation having the largest growth rate has a wavenumber which is moving towards small value as strain rate sensitivity rises. This effect has already been discussed in [9] for example and is retrieved with the

new approach. Moreover, Fig.10 validates the fact that for limited nominal strain rate, the classical theory based on a frozen coefficient theory is also valid for rate sensitive materials. Note that for larger nominal strain rates, as observed for the rate insensitive case, it has been checked that a difference still pertains even at large deformation.

It is also interesting to compare the evolution of the amplitude, as presented in Eq. (63), for different strain rate sensitivities. Only initial condition $IC6$ of Table 2 is considered here since trends are similar when adopting initial condition $IC5$. Fig. 11 shows the time evolution of the normalized amplitude for a perturbation whose wavenumber is $\gamma_1 = 85\pi/L_{01}$ (this wavenumber has been chosen because it presents a longer time period after reaching the Considère strain with moderate positive growth rate when compared to the case with the wavenumber $\gamma_1 = 23\pi/L_{01}$). The perturbation is more stable as m is increased. In fact, the perturbation growth rate being lower when m is large, see Fig. 10, the normalized amplitude of the perturbation starts to develop significantly later. Thus an increase in the strain rate sensitivity tends to delay the rapid growth of the perturbation. This trend reflects the stabilizing effect of viscosity, see for instance [9]. Note also that the oscillating behavior prior to the Considère strain observed for the rate insensitive case $m = 0$ is strongly reduced with the increase of the strain rate sensitivity. For $m = 0.05$, oscillations have totally disappeared, the amplitude of the perturbation decreases monotically until $t = 0.23\ ms$ and increases in a more controlled way for larger time. Note that with $m = 0.05$, the perturba-

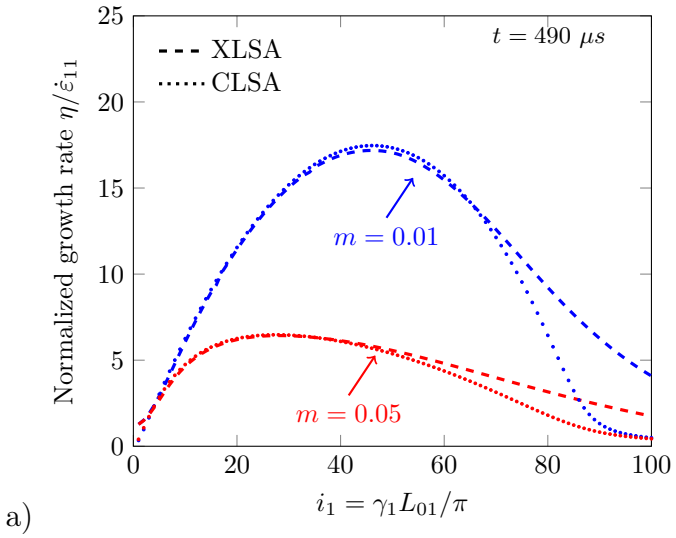

a)

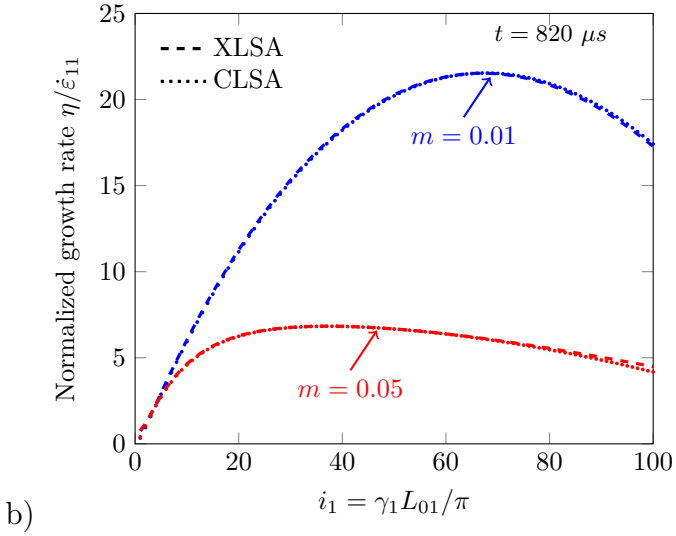

b)

Figure 10: Comparison of the normalized growth rate determined by the new approach and the Classical LSA. Results are displayed at a) $t = 490\ \mu s$ (nominal strain $\varepsilon_{11} = 0.49$) and b) $t = 820\ \mu s$ (nominal strain $\varepsilon_{11} = 0.82$). Initial condition IC6 of Table 2 is accounted for. The nominal strain rate is $\dot{\varepsilon}_{11} = 1000\ s^{-1}$. The material is rate sensitive and configuration of Fig. 9 is adopted. Two different strain rate sensitivities m are tested ($m = 0.01$ and $m = 0.05$).

tion has recovered its initial amplitude at $t = 0.65\ ms$ (corresponding plastic strain $\varepsilon_p = 0.58$). With the present results, one sees that even when the flow is stable, the perturbation amplitude may drastically changes. This could have some influence for the modeling of the fragmentation process where the amplitude of the defect can be at the origin of the inception of the fracture process. So a careful approach accounting for the history of the evolution is compulsory. The comparison of the predictions of the new model with finite element calculations is needed to validate the results and will be considered in a near future.

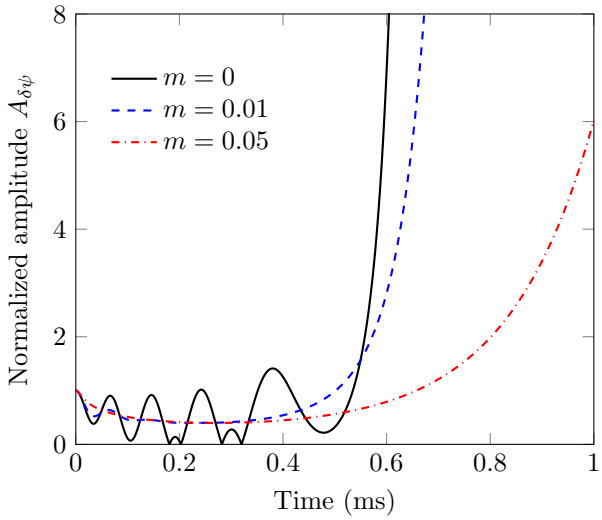

Figure 11: Normalized amplitude of a perturbation with wavenumber $\gamma_1 = 85\pi/L_{01}$ versus time. The nominal strain rate is $\dot{\varepsilon}_{11} = 1000\ s^{-1}$. The material is rate sensitive, with a flow stress described by Eq. (64) with $K = 1\ GPa$, $n = 0.2$ and $\dot{\varepsilon}_0 = 1\ s^{-1}$. The strain parameter is $\varepsilon_i = 0.1$. Various strain rate sensitivity parameters m are considered. Results for initial condition IC6 defined in Table 2 are only presented.

4.2.2. Thermo viscoplastic material

The full thermo-mechanical coupling is considered in this section where the material flow stress takes the form (see Eq. 56):

$$Y = K\left(\varepsilon_p + \varepsilon_i\right)^n \left(\frac{\dot{\varepsilon}_p}{\dot{\varepsilon}_0}\right)^m \left(\frac{\theta}{\theta_0}\right)^{-\beta} \tag{65}$$

Material parameters of section 4.2.1 are adopted : $K = 1\ GPa$, $n = 0.2$, $\dot{\varepsilon}_0 = 1\ s^{-1}$, $\varepsilon_i = 0.1$ and $m = 0.01$. In addition, thermal softening is accounted for with $\beta = 0.1$. The reference temperature is set to room temperature $\theta_0 = 293\ K$ and $\theta(t) > \theta_0$ for all $t > 0$ (thermal conduction has been neglected).

Since the material constitutive law is temperature sensitive, a strong thermo mechanical coupling exists. The extension of the linear stability analysis proposed in the present paper leads to a system of two equations which relates the mechanical part (42a) to the thermal part (42b). As a consequence, the perturbation is characterized by two distinct contributions : a mechanical perturbation $\tilde{\psi}$ and a thermal perturbation $\tilde{\theta}$. In the classical linear stability analysis, the thermal perturbation can be associated to the mechanical perturbation (stream function) via the assumption of frozen coefficient theory and the form given by Eq. 46, see [24].

For our new approach, an initial condition for the temperature is needed in addition to the two initial conditions for the mechanical part in $\tilde{\psi}$ and $\dot{\tilde{\psi}}$. In the previous section where the material was temperature insensitive, the

	$\tilde{\psi}(\tilde{X}_3, t_0 = 0)$	$\dot{\tilde{\psi}}(\tilde{X}_3, t_0 = 0)$	$\tilde{\theta}(\tilde{X}_3, t_0 = 0)$
$IC7$	$A_0\tilde{X}_3$	0	C_0

Table 3: Definition of the initial condition for the mechanical and thermal perturbations. The material constitutive response presents a thermo-mechanical coupling.

condition on the temperature was disregarded. We adopt the initial condition IC7, which is identical to IC5 of Table 2 for the mechanical part but includes an initial perturbation in temperature, see Table 3. We present here only the case of an initially uniform perturbation where $\tilde{\theta}(\tilde{X}_3, t_0 = 0) = C_0$, C_0 being a constant taken equal to 4 K. It has been checked that the value of the initial condition for $\tilde{\theta}$ has little influence on the development of the mechanical and thermal perturbations, at least when C_0 is small compared to θ_0. Note that non uniform initial perturbations in temperature have also been tested. Obtained results (not shown here) have revealed that the trends are preserved.

As in the previous section, the nominal strain rate is $\dot{\varepsilon}_{11} = 1000\ s^{-1}$ and results are presented for a perturbation with wavenumber $\gamma_1 = \frac{23\pi}{L_{01}}$. For the thermomechanical problem, the perturbation has two contributions which may present different growth rates. For the mechanical part, the growth rate η is defined in Eq. (60). A similar definition for the perturbation in temperature is adopted in this section:

$$\eta_T(t) = \frac{\dot{\tilde{\theta}}(\tilde{X}_3 = 1, t)}{\tilde{\theta}(\tilde{X}_3 = 1, t)} \tag{66}$$

The time evolution of the two normalized growth rates $\eta/\dot{\varepsilon}_{11}$ for the stream function and $\eta_T/\dot{\varepsilon}_{11}$ for the temperature perturbation is represented in Fig.12. Note that the growth rate derived from the classical linear stability analysis is unique for both mechanical and temperature evolutions. For $\dot{\varepsilon}_{11} = 1\,000\ s^{-1}$, the growth rate of the stream function η (mechanical part of the perturbation) and of the temperature perturbation η_T in the late deformation stage is close to the growth rate predicted by the classical approach. In the early stage of the deformation process, the two growth rates η and η_T are quite different. Note that this trend is not restricted to the considered wavenumber.

Since the perturbation has two contributions, we also define the normalized thermal amplitude by :

$$\mathrm{A}_{\delta\theta} = \frac{|\tilde{\theta}(\tilde{X}_3 = 1, t)|}{|\tilde{\theta}(\tilde{X}_3 = 1, t = 0)|} \tag{67}$$

Fig. 13 displays the normalized amplitude of the stream function $\mathrm{A}_{\delta\psi}$ given by Eq.(63) and that of the perturbed temperature $\mathrm{A}_{\delta\theta}$ as a function of the wavenumber index i_1 at $t = 260\ \mu s$ (plastic strain $\varepsilon_p = 0.27$). While in the classical approach, critical modes of the amplitude are identical for the stream function and the perturbed temperature (as only one growth rate is computed for all perturbed fields), the new model takes into account the thermo-mechanical coupling and reveals that in the early deformation stage, modes presenting the largest amplitude are slightly different for the stream

function and the perturbed temperature. In Fig. 13, the index of the critical mode for the mechanical perturbation is $i_1 = 28$ while for the temperature perturbation, $i_1 = 27$ ($t = 260\ \mu s$). For some particular modes (small or large values of i_1), there is no immediate correlation between the amplitudes of the mechanical and thermal perturbations. Indeed, it is seen that in some cases, the mechanical perturbation $\tilde{\psi}$ vanishes for particular modes (here $i_1 = 13$ or $i_1 = 82$ on Fig. 13) while the thermal perturbation $\tilde{\theta}$ has a non vanishing amplitude. The reverse situation is also observed for $i_1 = 9$ and $i_1 = 84$. These findings are time evolving. The situation depicted here will not be observed at larger time t, where the perturbation is highly unstable for any wavenumbers. In the late deformation stage, it has been checked that both critical modes are equal to the critical mode predicted by the CLSA model, at least for the nominal strain rate $\dot{\varepsilon}_{11} = 1000\ s^{-1}$. Indeed, Fig. 12 has clearly shown that the growth rate of the perturbed temperature and of the perturbed stream function are very close for large time t.

Influence of thermal softening is now discussed. The initial condition $IC7$ of Table 3 is still considered. Fig.14 presents the evolution of the normalized growth rate of a perturbation as a function of the wavenumber at $t = 1\ ms$ (nominal strain $\varepsilon_{11} = 1$) for $\beta = 0.1$ and $\beta = 0.2$. We display both the normalized mechanical growth rate $\eta_{/}\dot{\varepsilon}_{11}$ (Fig.14a) and the normalized thermal growth rate $\eta_T/\dot{\varepsilon}_{11}$ (Fig.14b) computed by the new approach and the one obtained using the classical approach (Eq.46). Remember that for the CLSA, by construction the same growth rate is governing the evolution

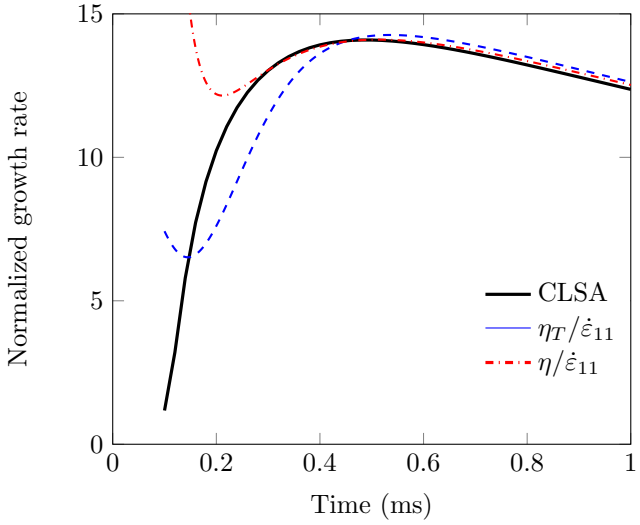

Figure 12: Normalized growth rates $\eta/\dot{\varepsilon}_{11}$ (see Eq.60) and $\eta_T/\dot{\varepsilon}_{11}$ (see Eq.66). The perturbations have the wave number $\gamma_1 = 23\pi/L_{01}$. The nominal strain rate is $\dot{\varepsilon}_{11} = 1000\ s^{-1}$. The material flow stress is given by Eq. (65). The rate sensitivity is $m = 0.01$. The thermal softening coefficient is $\beta = 0.1$ and $\theta_0 = 293\ K$. The strain parameter is $\varepsilon_i = 0.1$. Other parameters are defined in Fig. 9. Results are obtained with the initial condition IC7 of Table 3.

of all perturbed quantities. Fig.14 shows that the growth rates computed by the new approach converge to the growth rates computed by the classical approach regardless of the thermal softening coefficient for the presented wavenumbers. A slight difference still exists between η_T (growth rate for the thermal perturbation) and the growth rate evaluated by the CLSA, whereas an almost perfect match is found between η (growth rate for the mechanical perturbation) and the one provided by the CLSA. It is also seen that thermal softening destabilizes the flow since larger normalized growth rates are obtained for all wavenumbers when β is increased. This effect is well known in the literature (see [24] for example) and is retrieved with our extended

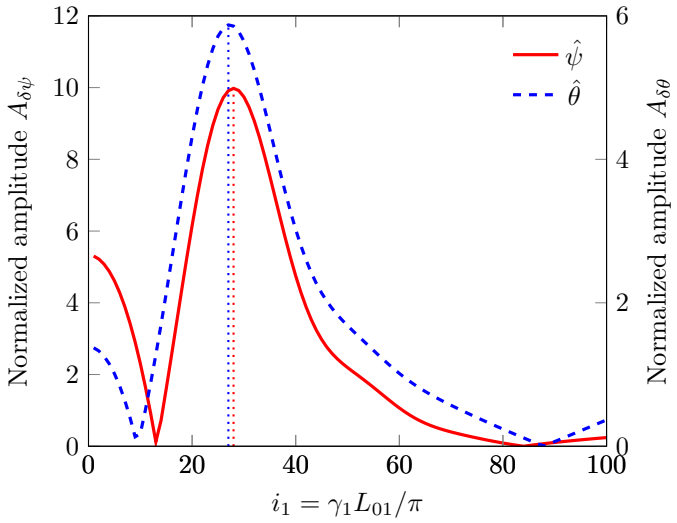

Figure 13: Normalized amplitude of the stream function and the perturbed temperature versus wavenumber at $t = 260$ μs (nominal strain $\varepsilon_{11} = 0.26$). The material flow stress is given by Eq. (65). The rate sensitivity is $m = 0.01$. The thermal softening coefficient is $\beta = 0.1$ and $\theta_0 = 293$ K. The strain parameter is $\varepsilon_i = 0.1$. Other parameters are defined in Fig. 9. Results are obtained with the initial condition IC7 of Table 3.

linear stability analysis without having to use the frozen coefficient theory. Note that for the two tested values of β, the growth rates η and η_T tends to be close at a large time. In particular, critical modes are the same for the thermal perturbation $\tilde{\theta}$ and the mechanical perturbation $\tilde{\psi}$.

4.3. Conclusion

A new model dedicated to the analysis of the linear stability of a plate under plain strain loading is proposed. Contrary to linear stability analyses of the literature, the assumption on the time dependency of the perturbation is no more enforced. The new linear stability analysis relaxes the previous assumption. It is observed that the frozen coefficient theory is no more a

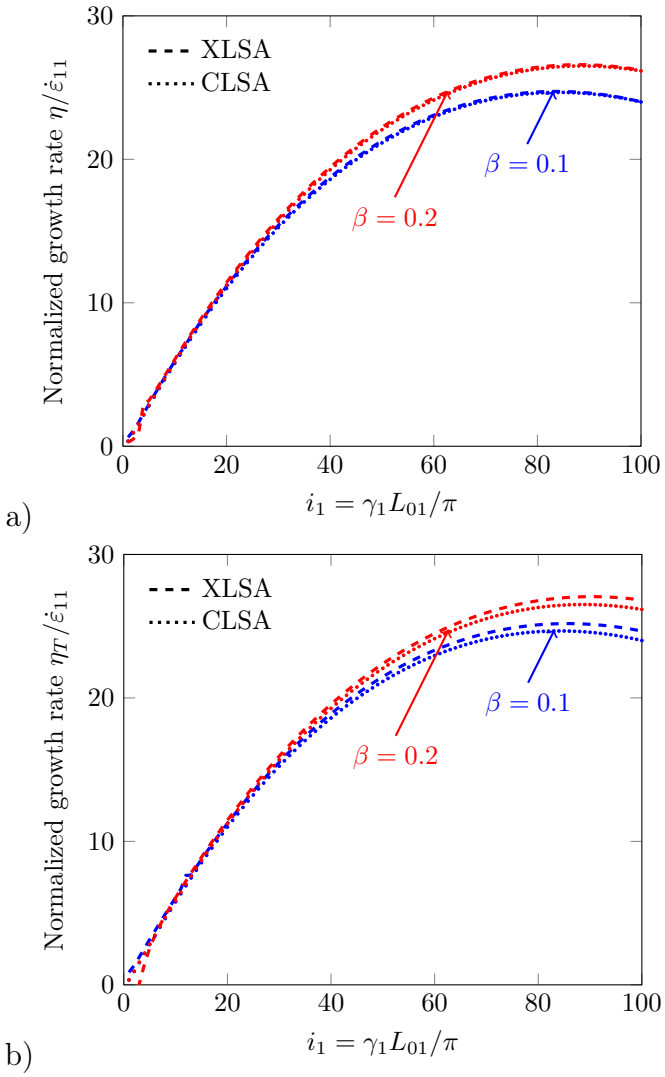

Figure 14: Normalized growth rates determined by the new approach a) $\eta/\dot{\varepsilon}_{11}$ (using Eq.(60)) b) $\eta_T/\dot{\varepsilon}_{11}$ (using Eq.(66)) and the Classical LSA (using Eq.(46)) versus wavenumber. Influence of the thermal softening parameter β. The initial condition is IC7 of Table 3. Results are obtained for a rate sensitive material presenting thermal softening, see Eq.(65). The considered time is $t = 1$ ms corresponding to a nominal strain $\varepsilon_{11} = 1$ since the nominal strain rate is $\dot{\varepsilon}_{11} = 1000\ s^{-1}$. Material parameters are $K = 1GPa$, $n = 0.2$, $m = 0.01$, $\dot{\varepsilon}_0 = 1\ s^{-1}$, $\beta = 0.1$, $\theta_0 = 293\ K$ and strain parameter $\varepsilon_i = 0.1$

necessity. For thermo mechanical problem, the perturbation has two contributions : one representative of the mechanical problem to represent the perturbation in position via the introduction of a stream function; the second one refers to the perturbed temperature. With the present method, no link between the two perturbations is imposed *a priori*.

The effect of initial conditions has been addressed in details in the paper. It is observed that for low strain rate loadings, the classical linear stability analysis and the new extension provide similar results, in terms of dominant modes and related growth rate (for large deformation). For high strain rate loading, the long term responses of the perturbation are seen to be consistent for both approaches, while at the early stage of the deformation, the dominant mode and more importantly the relative amplitude of the defects is really modified. The close agreement or not between the XLSA and the CLSA is depending whether the time scale separation exists or not between the perturbation and the background solution.

One of the main outcomes of the present approach is the fact that the evolution of the initial perturbation can be analyzed in the early stage of the deformation process (before the Considère criterion is met). This evolution is usually disregarded by the classical linear stability analyses. Such important finding needs to be validated by finite element calculations. This work is under development.

From the present approach, one can mention that depending on the ductility of the material, two situations can be distinguished. When the strain

to fracture is moderate, then the role of initial conditions on the growth rate of the perturbation is proeminent. We have seen that the dominant mode can be changed when adopting the XLSA formalism instead of the CLSA formalism. Consider now a material with a large failure strain. Then, it can be argued, based on the present results, that initial conditions for the perturbation will have a small effect on the multiple necking pattern. It has been shown that the dominant modes predicted by the CLSA and XLSA are consistent. Therefore, from the cases considered in the paper, the classical linear stability analysis provides an accurate estimate of the growth rate of the perturbation and of the dominant mode for most conditions.

AppendixA. Spectral method based on the Tau Method

In this Appendix, the Tau method is presented, see [3] for more details. Firstly, we recall some properties of the Chebyshev polynomials $T_i(x)$ of first order and of degree i. They are defined by the recurrence relation:

$$T_0(x) = 1 \tag{A.1a}$$

$$T_1(x) = x \tag{A.1b}$$

$$T_n(x) = 2xT_{n-1}(x) - T_{n-2}(x) \qquad \forall n \geq 2 \tag{A.1c}$$

It can be seen that:

$$T_i(x) = \cos\left(i \arccos\left(x\right)\right) \tag{A.2}$$

They form a basis for the space of real functions $u(x) : x \in [-1, 1] \to \mathbb{R}$. As a basis, a scalar product can be defined :

$$< T_i, T_j >= \int_{x=-1}^{x=1} T_i(x) T_j(x) p(x) dx \tag{A.3}$$

where $p(x)$ is the weight function :

$$p(x) = \frac{1}{\sqrt{1 - x^2}} \tag{A.4}$$

This basis is orthogonal :

$$< T_0, T_0 >= \pi \qquad < T_i, T_i >= \pi/2 \text{ for } i > 0 \qquad < T_i, T_j >= 0 \text{ for } i \neq j \tag{A.5}$$

Let us consider a function $u(x, t)$ expanded through a series of Chebyshev polynomials:

$$u(x, t) = \sum_{i=0}^{\infty} a_i(t) T_i(x) \tag{A.6}$$

For numerical purpose, the infinite sum in Eq. (A.6) is replaced by a truncated sum of order N :

$$u^N(x, t) = \sum_{i=0}^{N} a_i(t) T_i(x) \tag{A.7}$$

The vector $\mathbf{a} = (a_0(t) \ \ldots \ a_N(t))$ is the spectral representation of u^N.

The interpolation on the interval $[-1, 1]$ of the approximate u^N of the function u is based on the fixed Chebyshev grids. The Gauss-Lobatto-Chebyshev points are adopted here:

$$x_j = \cos\left(\frac{j\pi}{N}\right) \qquad 0 \leq j \leq N \tag{A.8}$$

These points are the extrema of the Chebyshev polynomial T_N (except for x_0 and x_N):

$$T_i(x_j) = \cos\left(\frac{ij\pi}{N}\right) \tag{A.9}$$

Let us define vector $\mathbf{v} = \left(u^N(x_0, t) \ \ldots \ u^N(x_N, t)\right)$ as the physical representation of u on the Gauss Lobatto set of points. From Eqs (A.7) and (A.9), a relationship between $\mathbf{v}$ and $\mathbf{a}$ is found:

$$\mathbf{v} = \mathbf{M}\mathbf{a} \tag{A.10}$$

with:

$$M_{ij} = T_i(x_j) = \cos\left(\frac{ij\pi}{N}\right) \tag{A.11}$$

Another important property of the Chebyshev polynomials is the possibility to calculate quite easily the partial derivatives of any function u. Indeed, since T_i is a polynomial of degree i, the k-th partial derivative $\frac{\partial^k T_i}{\partial x^k}$ is a polynomial of degree $i - k$ and can also be decomposed on the Chebyshev

basis. For instance, the first derivative of u^N can be expressed as

$$\frac{\partial u^N}{\partial x}(x,t) = \sum_{i=0}^{N} a_i^{(1)}(t) T_i(x) \tag{A.12}$$

The following notation has been used :

$$a^{(1)} = \mathbf{D_S} a \tag{A.13}$$

$\mathbf{D_S}$ is the first order spectral differentiation matrix, whose components are given by :

$$D_{S_{ij}} = \begin{cases} j & \text{if i=0 and j=1,3,5...} \\ 2j & \text{if i=1,2...,N-1 and j=i+1,i+3,...N} \\ 0 & \text{otherwise} \end{cases} \tag{A.14}$$

By definition, the first column is null, since it is associated with the first derivative of the constant term in the u^N expansion. Similarly, the last line is also null. Indeed, u^N being a N-th order polynomial, its derivative is a polynomial of degree $(N-1)$. Hence, the coefficient $a_N^{(1)}$ associated with the degree N in the derivative is equal to 0. Spectral coefficients $a^{(p)}$ of $\frac{\partial^p u}{\partial x^p}(x,t)$ are computed through the relationship :

$$a^{(p)} = \mathbf{D_S^p} a \tag{A.15}$$

Secondly, let us consider the following differential equation on u defined

on the space domain Ω:

$$Au = f \tag{A.16}$$

with A being a differential operator containing derivatives up to the k-th order. The system is complemented by boundary conditions on the frontier $\partial\Omega$. Let us denote by u^N the Chebyshev expansion of u, truncated at the order N. The residual R^N of the system can also be expanded as a series of Chebyshev polynomials :

$$R^N = Au^N - f^N = A\left(\sum_{i=0}^{N} a_i T_i\right) - \sum_{i=0}^{N} f_i T_i \tag{A.17}$$

with f^N being the Chebyshev polynomial expansion of f The goal is to minimize this residual. Note that for the exact solution of the problem, the residual should vanish. In the Tau method, spectral coefficients a_i are determined such that the residual is orthogonal to all Chebyshev polynomials. With that definition, the scalar product between the residual and the Chebyshev polynomials is zero :

$$< R^N, T_i >= 0 \quad \text{for } i = 0, ..., N-k \tag{A.18}$$

The use of Eq. (A.18) leads to Eq. (53).

Since the operator A contains derivatives up to the k-th order, a system of $N - k + 1$ time differential equations is formed, the solutions being the spectral coefficients a_i. Then k boundary conditions are needed for com-

pleteness of the system. The boundary conditions are expressed based on the Chebyshev approximation u^N. Finally, a system of $N+1$ equations for the $N+1$ unknowns a_i is found. When the functions a_i are found, the value of vector $\mathbf{v}$ is obtained by Eq. (A.10). When N is large enough, then a good approximation for u is obtained.

AppendixB. Time discretization of the set of Equations

In the following, we define $t^n = t_0 + ndt$ and for any function u, $u^n = u(t^n)$. Time derivatives are evaluated with finite difference scheme :

$$\begin{cases} \dfrac{\partial u}{\partial t}(t^n) = \dfrac{u^n - u^{n-1}}{dt} & \text{(B.1a)} \\ \\ \dfrac{\partial^2 u}{\partial t^2}(t^n) = \dfrac{u^n - 2u^{n-1} + u^{n-2}}{dt^2} & \text{(B.1b)} \end{cases}$$

A staggered time grid is considered. Indeed, the functions q_i of the spectral representation of the stream function are evaluated at time $t^{n+\frac{1}{2}}$ while the functions p_i of the spectral representation of the temperature perturbation are evaluated at time t^n. Assume that spectral decompositions of the stream function and temperature perturbation are known quantities up to t^n. With a time splitting strategy, each timestep dt (dt is fixed) is split in two substeps. Based on the implicit finite difference scheme, it is shown that :

1. From mechanical equation (53) and boundary conditions (55), $\mathbf{q}^{n+\frac{1}{2}}$ is computed owing to $\mathbf{q}^{n-\frac{1}{2}}$, $\mathbf{q}^{n-\frac{3}{2}}$ and $\mathbf{p}^n$

2. From heat equation (54), $\mathbf{p}^{n+1}$ is computed owing to $\mathbf{p}^{n}$, $\mathbf{q}^{n+\frac{1}{2}}$ and $\mathbf{q}^{n-\frac{1}{2}}$

More precisely, with the introduction of the spectral derivative matrix $\mathbf{D_S}$ (see AppendixA), mechanical equation 53 and boundary conditions 55 are written in a matricial form:

$$\mathbf{U^{n+\frac{1}{2}}q}^{n+\frac{1}{2}} = \mathbf{U^{n-\frac{1}{2}}q}^{n-\frac{1}{2}} + \mathbf{U^{n-\frac{3}{2}}q}^{n-\frac{3}{2}} + \mathbf{V^{n}p}^{n} \tag{B.2}$$

Note that, the truncation order for the stream function is N while for the temperature perturbation, the order is $N-1$. For representative convenience, we imposed the N^{th} component of the temperature perturbation to be equal to zero $p_N = 0$. Therefore, both vectors $\mathbf{p}$ and $\mathbf{q}$ have the same number of components and all matrices used in the subsequent of the appendix are

square matrix (N+1 lines and N+1 columns).

$$U_{ij}^{n+\frac{1}{2}} = \begin{cases} \frac{a_1}{L_{03}^2 dt^2} D_{S_{ij}}^2 + \frac{a_2}{dt^2}\delta_{ij} + \frac{a_3}{L_{03}^4 dt} D_{S_{ij}}^4 + \frac{a_4}{L_{03}^2 dt} D_{S_{ij}}^2 + \frac{a_5}{dt}\delta_{ij} + \frac{a_6}{L_{03}^2} D_{S_{ij}}^2 & (i \leq N-4) \\ \frac{1}{L_{03}^2 dt} \sum_{k=0}^{N} D_{S_{kj}}^2 + \frac{c_1}{dt} - \gamma_1 c_2 & (i = N-3) \\ \frac{1}{L_{03}^2 dt} \sum_{k=0}^{N} (-1)^k D_{S_{kj}}^2 + (-1)^j \left(\frac{c_1}{dt} - \gamma_1 c_2 \right) & (i = N-2) \\ \frac{n_1}{L_{03} dt^2} \sum_{k=0}^{N} D_{S_{kj}} + \frac{n_2}{L_{03}^3 dt} \sum_{k=0}^{N} D_{S_{kj}}^3 + \frac{n_3}{L_{03} dt} \sum_{k=0}^{N} D_{S_{kj}} + \frac{n_4}{L_{03}} \sum_{k=0}^{N} D_{S_{kj}} + n_5 & (i = N-1) \\ \frac{n_1}{L_{03} dt^2} \sum_{k=0}^{N} (-1)^k D_{S_{kj}} + \frac{n_2}{L_{03}^3 dt} \sum_{k=0}^{N} (-1)^k D_{S_{kj}}^3 + \frac{n_3}{L_{03} dt} \sum_{k=0}^{N} (-1)^k D_{S_{kj}} & \\ + \frac{n_4}{L_{03}} \sum_{k=0}^{N} (-1)^k D_{S_{kj}} + (-1)^j n_5 & (i = N) \end{cases}$$

Note that the index j is varying in the range $[0, N]$.

$$U_{ij}^{n-\frac{1}{2}} = \begin{cases} \frac{2a_1}{L_{03}^2 dt^2} D_{S_{ij}}^2 + \frac{2a_2}{dt^2}\delta_{ij} + \frac{a_3}{L_{03}^4 dt} D_{S_{ij}}^4 + \frac{a_4}{L_{03}^2 dt} D_{S_{ij}}^2 + \frac{a_5}{dt}\delta_{ij} & (i \leq N-4) \\ \frac{1}{L_{03}^2 dt} \sum_{k=0}^{N} D_{S_{kj}}^2 + \frac{c_1}{dt} & (i = N-3) \\ \frac{1}{L_{03}^2 dt} \sum_{k=0}^{N} (-1)^k D_{S_{kj}}^2 + (-1)^j \frac{c_1}{dt} & (i = N-2) \\ \frac{2n_1}{L_{03} dt^2} \sum_{k=0}^{N} D_{S_{kj}} + \frac{n_2}{L_{03}^3 dt} \sum_{k=0}^{N} D_{S_{kj}}^3 + \frac{n_3}{L_{03} dt} \sum_{k=0}^{N} D_{S_{kj}} & (i = N-1) \\ \frac{2n_1}{L_{03} dt^2} \sum_{k=0}^{N} (-1)^k D_{S_{kj}} + \frac{n_2}{L_{03}^3 dt} \sum_{k=0}^{N} (-1)^k D_{S_{kj}}^3 + \frac{n_3}{L_{03} dt} \sum_{k=0}^{N} (-1)^k D_{S_{kj}} & (i = N) \end{cases}$$

$$U_{ij}^{n-\frac{3}{2}} = \begin{cases} -\dfrac{a_1}{L_{03}^2 dt^2} D_{S_{ij}}^2 - \dfrac{a_2}{dt^2}\delta_{ij} & (i \leq N-4) \\ 0 & (i = N-3) \\ 0 & (i = N-2) \\ -\dfrac{n_1}{L_{03} dt^2} \displaystyle\sum_{k=0}^{N} D_{S_{kj}} & (i = N-1) \\ -\dfrac{n_1}{L_{03} dt^2} \displaystyle\sum_{k=0}^{N} (-1)^k D_{S_{kj}} & (i = N) \end{cases}$$

$$V_{ij}^{n} = \begin{cases} -\dfrac{a_7}{L_{03}} D_{S_{ij}} & (i \leq N-4) \\ 0 & (i = N-3) \\ 0 & (i = N-2) \\ -n_6 & (i = N-1) \\ -(-1)^j n_6 & (i = N) \end{cases}$$

From Eq. (B.2), the recurrence relation for the spectral representation $\mathbf{q}^{n+\frac{1}{2}}$ of the stream function is provided at time $t^{n+\frac{1}{2}}$:

$$\mathbf{q}^{n+\frac{1}{2}} = \left(\mathbf{U^{n+\frac{1}{2}}}\right)^{-1} \mathbf{U^{n-\frac{1}{2}}} \mathbf{q}^{n-\frac{1}{2}} + \left(\mathbf{U^{n+\frac{1}{2}}}\right)^{-1} \mathbf{U^{n-\frac{3}{2}}} \mathbf{q}^{n-\frac{3}{2}} + \left(\mathbf{U^{n+\frac{1}{2}}}\right)^{-1} \mathbf{V^{n}} \mathbf{p}^{n} \tag{B.3}$$

With the same strategy, the discretization of Eq. (54) provides an expression for the spectral representation of the temperature perturbation at

time t_{n+1}, $\mathbf{p}^{n+1}$:

$$\mathbf{p}^{n+1} = \frac{1}{1+b_1 dt}\left(\mathbf{p}^n - \frac{b_2 + b_3 dt}{L_{03}}\mathbf{D_S q}^{n+\frac{1}{2}} + \frac{b_2}{L_{03}}\mathbf{D_S q}^{n-\frac{1}{2}}\right) \tag{B.4}$$

Since system (42) with boundary conditions (44) is a system of time differential equations with second order time derivatives on $\tilde{\psi}$ and first order time derivatives on $\tilde{\theta}$, initial conditions on the spectral coefficients ($\mathbf{q}(t_0 = 0)$, $\dot{\mathbf{q}}(t_0 = 0)$ and $\mathbf{p}(t_0 = 0)$) are needed. For the finite difference scheme, it is necessary to provide values for $\mathbf{q}^{-\frac{3}{2}}$, $\mathbf{q}^{-\frac{1}{2}}$ et $\mathbf{p}^0$ vectors.

AppendixC. Case of the frozen coefficient theory

The system (42) with boundary conditions (44) could be integrated assuming that the unknowns (mechanical stream function and temperature perturbation) have the following shape :

$$\tilde{\psi}(\tilde{X}_3, t) = \tilde{\psi}^{CLSA}(\tilde{X}_3, t) = Ae^{\eta t}e^{i\tilde{l}\tilde{X}_3} \qquad \tilde{\theta}(\tilde{X}_3, t) = \tilde{\theta}^{CLSA}(\tilde{X}_3, t) = Be^{\eta t}e^{i\tilde{l}\tilde{X}_3} \tag{C.1}$$

together with the frozen coefficient assumption. In that case, the equations of the linear stablity analysis proposed in [25] or [24] are retrieved.

Indeed, the system (42) together with the proposed form (C.1) becomes :

$$\frac{a_1}{L_{03}^2}\eta^2\tilde{\psi}_{,33} + a_2\eta^2\tilde{\psi} + \frac{a_3}{L_{03}^4}\eta\tilde{\psi}_{,3333} + \frac{a_4}{L_{03}^2}\eta\tilde{\psi}_{,33} + a_5\eta\tilde{\psi} + \frac{a_6}{L_{03}^2}\tilde{\psi}_{,33} + \frac{a_7}{L_{03}}\tilde{\theta}_{,3} = 0 \tag{C.2}$$

$$\eta\tilde{\theta} + b_1\tilde{\theta} + \frac{b_2}{L_{03}}\eta\tilde{\psi}_{,3} + \frac{b_3}{L_{03}}\tilde{\psi}_{,3} = 0 \tag{C.3}$$

From Eq.(C.3), the perturbation of the temperature is expressed in terms of the stream function $\tilde{\psi}$:

$$\tilde{\theta} = -\frac{1}{\eta + b_1}(b_2\eta + b_3)\frac{1}{L_{03}}\tilde{\psi}_{,3} = \frac{\tilde{b}}{L_{03}}\tilde{\psi}_{,3} \tag{C.4}$$

With the definition of b_2 and b_3 given in Eq.(43), the coefficient $\tilde{b}$ is expressed as :

$$\tilde{b} = -\frac{1}{\eta - \dfrac{Y_{,\dot{\theta}}^{(b)}\dot{\varepsilon}_p^{(b)}}{\rho C}}\left(\frac{2\eta\gamma_1}{\sqrt{3}\rho C}\left[Y_{,\dot{\varepsilon}_p}^{(b)}\dot{\varepsilon}_p^{(b)} + Y^{(b)}\right] + \frac{2\gamma_1}{\sqrt{3}\rho C}Y_{,\varepsilon_p}^{(b)}\dot{\varepsilon}_p^{(b)}\right) \tag{C.5}$$

The coefficient $\tilde{b}$ is related to the coefficient $\tilde{C}$ obtained in [24] since for the frozen coefficient theory, the relation between the perturbation in strain and the stream function given by Eq. (26) prevails:

$$\tilde{C} = -\tilde{b}\frac{\sqrt{3}}{2\gamma_1\eta} \tag{C.6}$$

Next, the relationship (C.4) being introduced into Eq.(C.2), the fourth order partial differential equation as presented in [24] is obtained. With definition (C.1), a polynomial equation for l is obtained :

$$\alpha_4 \tilde{l}^4 / L_{03}^4 + \alpha_2 \tilde{l}^2 / L_{03}^2 + \alpha_0 = 0 \tag{C.7}$$

with:

$$\alpha_4 = \eta a_3 \quad \alpha_2 = -\eta^2 a_1 - \eta a_4 - a_6 - a_7 \tilde{b} \quad \alpha_0 = \eta^2 a_2 + \eta a_5 \tag{C.8}$$

The dispersion relation (C.7) is identical to the one of [24].

For each value of η, four values of transversal modes $\tilde{l}$ are obtained (see [25] or [24] for more details). As a consequence, the solution is a linear combination of the four transversal modes and must satisfy the boundary conditions (44). From this appendix, we clearly see that, the new approach contains also the case of the frozen coefficient theory but is more general.

[1] Altynova, M., Hu, X., Daehn, G. S., 1996. Increased ductility in high velocity electromagnetic ring expansion. Met. and Mat. Trans. 27A, 1837–1844.

[2] Becker, R., 2002. Ring fragmentation predictions using the Gurson model with material stability conditions as failure criterion. Int. J. Solids Struct. 39, 3555–3580.

[3] Canuto, C., Hussaini, M. Y., Quarteroni, A. M., Thomas Jr, A., et al.,

2012. Spectral methods in fluid dynamics. Springer Science & Business Media.

[4] Considère, A., 1885. Mémoire sur l'emploi du fer et de l'acier dans les constructions. Annales des Ponts et Chaussées 9 (34), 574–775.

[5] Dequiedt, J. L., 2015. Statistics of dynamic fragmentation for a necking instability. International Journal of Solids and Structures 75-76, 32–44.

[6] El Maï, S., Mercier, S., Petit, J., Molinari, A., 2014. An extension of the linear stability analysis for the prediction of multiple necking during dynamic extension of round bar. International Journal of Solids and Structures 51, 3491–3507.

[7] Fressengeas, C., Molinari, A., 1985. Inertia and thermal effects on the localization of plastic flow. Acta Metall. 33, 387–396.

[8] Fressengeas, C., Molinari, A., 1987. Instability and localization of plastic flow in shear at high strain rates. Journal of the Mechanics and Physics of Solids 35, 185–211.

[9] Fressengeas, C., Molinari, A., 1994. Fragmentation of rapidly stretching sheets. Eur. J. Mech. A/Solids 13, 251–268.

[10] Fyfe, I. M., Rajendran, A. M., 1980. Dynamic pre-strain and inertia effects on the fracture of metals. J. Mech. Phys. Solids 28, 17–26.

[11] Goto, D. M., Becker, R., Orzechowski, T. J., Springer, H. K., Sunwoo, A., Syn, C., 2008. Investigation of the fracture and fragmentation of explosively driven rings and cylinders. Int. J. Impact. Eng. 35, 1547–1556.

[12] Grady, D. E., Benson, D. A., 1983. Fragmentation of metal rings by electromagnetic loading. Exp. Mech. 12, 393–400.

[13] Grady, D. E., Olsen, M. L., 2003. A statistics and energy based theory of dynamic fragmentation. Int. J. Impact. Eng. 29, 293–306.

[14] Guduru, P. R., Freund, L. B., 2002. The dynamics of multiple neck formation and fragmentation in high rate extension of ductile materials. Int. J. Solids Struct. 39, 5615–5632.

[15] Hill, R., Hutchinson, J. W., 1975. Bifurcation phenomena in the plane tension test. J. Mech. Phys. Solids 23, 239–264.

[16] Hoggatt, C. R., Recht, R. F., 1968. Fracture behavior of tubular bombs. J. Appl. Phys. 39, 1856–1862.

[17] Hutchinson, J. W., Neale, K. W., Needleman, A., 1978. Sheet necking I- validity of plane stress assumptions on the long wavelength approximation. In: Koistinen, D. P., Wang, N. M. (Eds.), Mechanics of Sheet Metal Forming. Plenum, N. Y., pp. 111–126.

[18] Jeanclaude, V., Fressengeas, C., 1997. Dynamic necking of rods at high strain rates. J. Phys. IV Colloque C3 7, 699–704.

[19] Jouve, D., 2010. Etude analytique de l'instabilité plastique de striction pour une plaque sollicitée en traction biaxiale. Ph.d. thesis, Ecole Polytechnique, France.

[20] Jouve, D., 2013. Analytic study of plastic necking instabilities during plane tension tests. European Journal of Mechanics A/Solids 39, 180–196.

[21] Jouve, D., 2015. Analytic study of the onset of plastic necking instabilities during biaxial tension tests on metallic plates. European Journal of Mechanics A/Solids 50, 59–69.

[22] Lanczos, C., 1938. Trigonometric interpolation of empirical and analytical functions. Journal of Mathematics and Physics 17 (1-4), 123–199.

[23] Llorca, F., Juanicotena, A., 1997. Expanding ring test: numerical simulation - application to the analysis of experimental data. J. PHYS IV FRANCE 7 3, 235–240.

[24] Mercier, S., Granier, N., Molinari, A., Llorca, F., Buy, F., 2010. Multiple necking during the dynamic expansion of hemispherical metallic shells, from experiments to modelling. J. Mech. Phys. Sol. 58 (7), 955–982.

[25] Mercier, S., Molinari, A., 2003. Predictions of bifurcation and instabilities during dynamic extension. Int. J. Solids Struct. 40, 1995–2016.

[26] Mercier, S., Molinari, A., 2004. Analysis of multiple necking in rings under rapid radial expansion. Int. J. Impact Eng. 30, 403–419.

[27] Mott, N. F., 1947. Fragmentation of shell cases. In: Proceedings of The Royal Society. Series A. pp. 300–308.

[28] Niordson, F. I., 1965. A unit for testing materials at high strain rates. Exp. Mech. 5, 29–32.

[29] Olive, F., Nicaud, A., Marilleau, J., Loichot, R., 1979. Rupture behaviour of metals in explosive expansion. Inst. Phys. Conf. Ser. 47, 242–251.

[30] Pandolfi, A., Krysl, P., Ortiz, M., 1999. Finite element simulation of ring expansion and fragmentation. Int. J. Fract. 95, 279–297.

[31] Petit, J., Jeanclaude, V., Fressengeas, C., 2005. Breakup of copper shaped-charge jets: Experiments, numerical simulations, and analytical modeling. J. Appl. Physics 98, 123521.

[32] Ravi-Chandar, K., Triantafyllidis, N., 2015. Dynamic stability of a bar under high loading rate: Response to local perturbations. International Journal of Solids and Structures 58, 301–308.

[33] Rodríguez-Martínez, J. A., Vadillo, G., Fernández-Sáez, J., Molinari, A., 2013b. Identification of the critical wavelength responsible for the fragmentation of ductile rings expanding at very high strain rates. Journal of the Mechanics and Physics of Solids 61, 1357–1376.

[34] Rodríguez-Martínez, J. A., Vadillo, G., Zaera, R., Fernández-Sáez, J., 2013a. On the complete extinction of selected imperfection wavelengths

in dynamically expanded ductile rings. Mechanics of Materials 60, 107–120.

[35] Rusinek, A., Zaera, R., 2007. Finite element simulation of steel ring fragmentation under radial expansion. Int. J. Impact Eng. 34, 799–822.

[36] Shenoy, V. B., Freund, L. B., 1999. Necking bifurcations during high strain rate extension. J. Mech. Phys. Solids 47, 2209–2233.

[37] Slate, P. M. B., Billings, M. J. W., Fuller, P. J. A., 1967. The rupture behaviour of metals at high strain rates. J. Inst. Metals 95, 244–251.

[38] Vaz-Romero, A., Rodríguez-Martínez, J. A., Mercier, S., Molinari, A., 2017. Multiple necking pattern in nonlinear elastic bars subjected to dynamic stretching: The role of defects and inertia. International Journal of Solids and Structures 125, 232 – 243.

[39] Wesenberg, D., Sagartz, M., 1977. Dynamic fracture of 6061-T6 aluminium cylinders. J. Appl. Mech. 44, 643–646.

[40] Xue, Z., Vaziri, A., Hutchinson, J. W., 2008. Material aspects of dynamic neck retardation. J. Mech. Phys. Solids 56, 93–113.

[41] Zhang, H., Ravi-Chandar, K., 2006. On the dynamics of necking and fragmentation- I. Real-time and post-mortem observations in Al 6061-O. Int. J. Fract. 142, 183–217.

[42] Zhang, H., Ravi-Chandar, K., 2008. On the dynamics of necking and fragmentation- II. effect of material properties, geometrical constraints and absolute size. Int. J. Fract. 150, 3–36.

[43] Zhang, H., Ravi-Chandar, K., 2010. On the dynamics of localization and fragmentation- IV. expansion of al 6061-o tubes. Int. J. Fract. 163, 41–65.

[44] Zhou, F., Molinari, J. F., Ramesh, K. T., 2006. An elastic-visco-plastic analysis of ductile expanding ring. Int. J. Impact Eng. 33, 880–891.